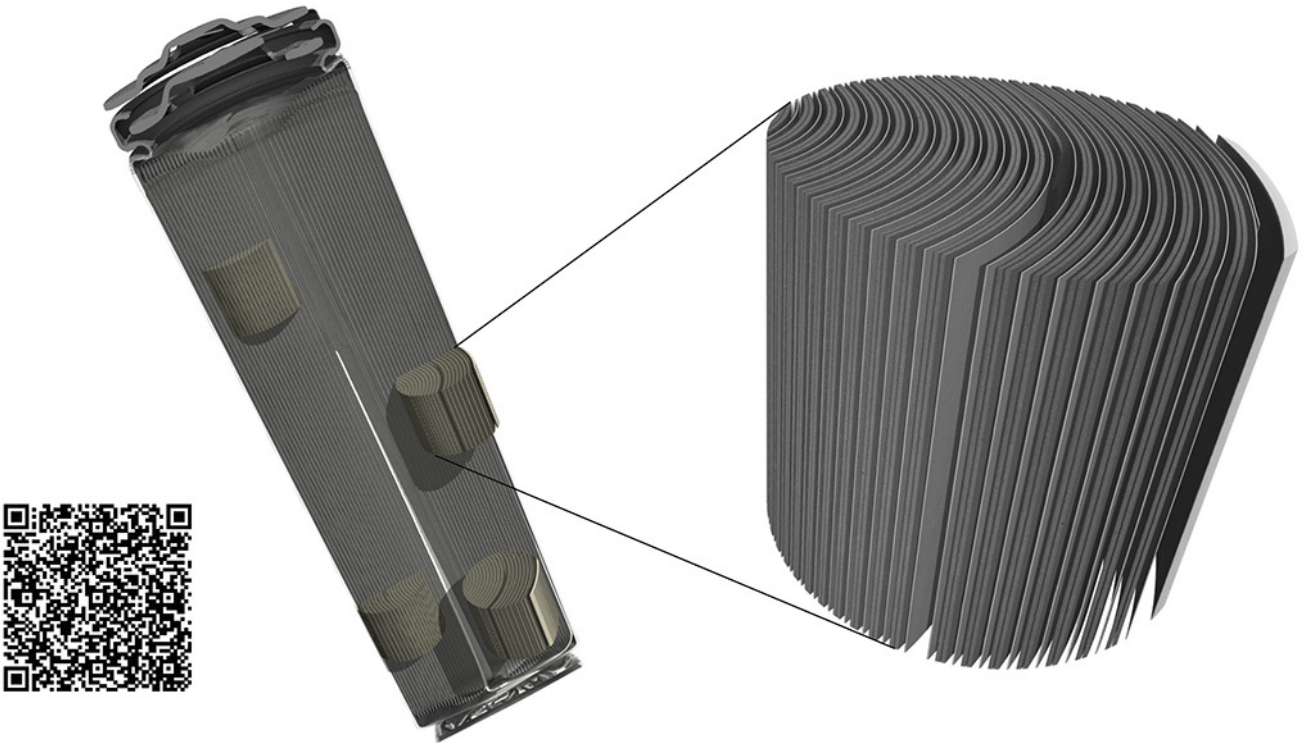


## TESCAN micro-CT solutions

## for energy storage materials research



## TESCAN UniTOM XL

- ✓ Multi-scale non-destructive 3D imaging optimized to maximize throughput and contrast
- ✓ Fast scanning and high sample throughput with temporal resolutions below 10 seconds
- ✓ Wide array of samples types
- ✓ Enables dynamic tomography and *in-situ* experiments
- ✓ Dynamic screening for synchrotron beamtime
- ✓ Modular and open system with unmatched flexibility for research



[Click and find out more](#)

# Lithium Oxide Superionic Conductors Inspired by Garnet and NASICON Structures

Yihan Xiao, Kyujung Jun, Yan Wang, Lincoln J. Miara, Qingsong Tu, and Gerbrand Ceder\*

The key component in lithium solid-state batteries (SSBs) is the solid electrolyte composed of lithium superionic conductors (SICs). Lithium oxide SICs offer improved electrochemical and chemical stability compared with sulfides, and their recent advancements have largely been achieved using materials in the garnet- and NASICON (sodium superionic conductor)-structured families. In this work, using the ion-conduction mechanisms in garnet and NASICON as inspiration, a common pattern of an “activated diffusion network” and three structural features that are beneficial for superionic conduction: a 3D percolation Li diffusion network, short distances between occupied Li sites, and the “homogeneity” of the transport path are identified. A high-throughput computational screening is performed to search for new lithium oxide SICs that share these features. From this search, seven candidates are proposed exhibiting high room-temperature ionic conductivity evaluated using *ab initio* molecular dynamics simulations. Their structural frameworks including spinel, oxy-argyrodite, sodalite, and  $\text{LiM}(\text{SeO}_3)_2$  present new opportunities for enriching the structural families of lithium oxide SICs.

of a relatively wide electrochemical stability window,<sup>[3–6]</sup> good chemical stability with oxide cathode materials,<sup>[3–6]</sup> and good thermal stability.<sup>[7]</sup> To date, the best performance of oxide SEs in high-energy-density SSBs has largely come from two structural families: cubic-garnet-structured  $\text{Li}_x\text{A}_3\text{B}_2\text{O}_{12}$  (A = La, Nd, Mg, Ba, etc., B = Te, Ta, Nb, Zr, In, etc.)<sup>[8]</sup> and NASICON (sodium superionic conductor)-structured  $\text{Li}_{1-x}\text{A}_x\text{B}_{2-x}(\text{PO}_4)_3$  (A = Al, La, In, Cr, etc., B = Ti, Ge, Zr, Hf, Sn, etc.).<sup>[9]</sup> Other oxide SEs such as LiPON (lithium phosphorus oxynitride),<sup>[10]</sup> antiperovskites  $\text{Li}_3\text{OX}$  (X = Cl or Br),<sup>[11]</sup> perovskites  $\text{Li}_{3x}\text{La}_{2/3-x}\text{TiO}_3$ ,<sup>[12]</sup> and LISICONs (lithium superionic conductors) with the  $\gamma\text{-Li}_3\text{PO}_4$  framework (e.g.,  $\text{Li}_{2+2x}\text{Zn}_{1-x}\text{GeO}_4$ )<sup>[13,14]</sup> have been used less frequently because of their relatively low ionic conductivity,<sup>[2]</sup> poor electrochemical stability against a Li metal anode,<sup>[4]</sup> or difficulty in synthesizing pure-phase materials.<sup>[15,16]</sup>

## 1. Introduction

Solid electrolytes (SEs) composed of lithium superionic conductors (SICs) with ionic conductivities higher than  $0.1 \text{ mS cm}^{-1}$  are the key component of lithium solid-state batteries (SSBs).<sup>[1,2]</sup> Among the various categories of SEs, oxides have the advantages

In contrast, sulfide SEs with various structure types have been developed and widely applied in lithium SSBs, including  $\text{Li}_2\text{S-P}_2\text{S}_5$  glass,<sup>[17]</sup>  $\text{Li}_7\text{P}_3\text{S}_{11}$  glass-ceramics,<sup>[18]</sup>  $\text{Li}_{10}\text{GeP}_2\text{S}_{12}$ ,<sup>[19]</sup> and its derivatives,<sup>[20,21]</sup> argyrodites  $\text{Li}_6\text{PS}_5\text{X}$  (X = Cl, Br, or I),<sup>[22–24]</sup>  $\beta\text{-Li}_3\text{PS}_4$ ,<sup>[25,26]</sup> and  $\text{Li}_{1+2x}\text{Zn}_{1-x}\text{PS}_4$ .<sup>[27–29]</sup> Moreover, the ionic conductivity of oxide SEs is generally at least one order of magnitude lower than that of sulfide SEs.<sup>[2]</sup> Therefore, it is important to discover new lithium oxide SICs with new structural frameworks and high room-temperature ionic conductivity ( $\sigma_{\text{it}}$ ) for further development of oxide-SE-based SSBs.


Over the past 60 years, only six structural families of lithium oxide SICs have been discovered:<sup>[30,31]</sup>  $\beta$ -alumina (1960s),<sup>[32]</sup> NASICONs (1970s),<sup>[33,34]</sup> LISICONs (1970s),<sup>[13]</sup> perovskites (1990s),<sup>[35]</sup> garnets (2000s),<sup>[36,37]</sup> and antiperovskites (2000s–2010s).<sup>[11,38]</sup> Since the discovery of the prototype compounds in each family, their ionic conductivity, stability, and processability have been optimized through experimental and computational efforts.<sup>[8,12,20,21]</sup> However, the broader exploration of the structural space of oxides with the aim to discover new frameworks for lithium oxide SICs is difficult as few guiding principles exist for what makes a fast Li-ion conductor.

Recently, computational studies of known lithium SICs using first-principles methods have shed light on some mechanisms and features that can individually or synergistically lead to superionic conduction, such as polarizable anions,<sup>[39]</sup> a bcc anion framework,<sup>[40]</sup> the cooperative motion of Li ions,<sup>[41,42]</sup> a frustrated Li sublattice,<sup>[43]</sup> and enlarged Li sites.<sup>[44]</sup> This mechanistic understanding of Li-ion conduction can guide the design

Y. Xiao,<sup>[\*]</sup> K. Jun, G. Ceder  
Department of Materials Science and Engineering  
University of California  
Berkeley, CA 94720, USA  
E-mail: gceder@berkeley.edu

Y. Xiao, K. Jun, Q. Tu, G. Ceder  
Materials Sciences Division  
Lawrence Berkeley National Laboratory  
Berkeley, CA 94720, USA

Y. Wang, L. J. Miara  
Advanced Materials Lab  
Samsung Research America  
10 Wilson Rd, Cambridge, MA 02138, USA

 The ORCID identification number(s) for the author(s) of this article can be found under <https://doi.org/10.1002/aenm.202101437>.

© 2021 The Authors. Advanced Energy Materials published by Wiley-VCH GmbH. This is an open access article under the terms of the Creative Commons Attribution-NonCommercial License, which permits use, distribution and reproduction in any medium, provided the original work is properly cited and is not used for commercial purposes.

<sup>[\*]</sup>Present address: Facebook Inc., 1 Hacker Way, Menlo Park, CA 94025, USA

DOI: 10.1002/aenm.202101437

of ionic conductors<sup>[40,42,44]</sup> and has led to some predictions of new SIC candidates with structural frameworks dissimilar to those of known SICs.<sup>[44,45]</sup> Successful examples that have been validated by experiments include  $\text{Li}_{1+2x}\text{Zn}_{1-x}\text{PS}_4$  ( $\sigma_{\text{rt}} = 3.5 \times 10^{-3} \text{ S cm}^{-1}$ ),<sup>[28,29,46]</sup> predicted based on its bcc anion framework feature,<sup>[28,40]</sup> and  $\text{Li}_{1+x}\text{Ta}_{1-x}\text{Zr}_x\text{SiO}_5$  ( $\sigma_{\text{rt}} = 2.97 \times 10^{-5} \text{ S cm}^{-1}$ ),<sup>[47,48]</sup> predicted based on its enlarged lithium site feature.<sup>[42,44]</sup> These feature-based computational search strategies allow for efficient and widespread exploration of the structural space as compared to more traditional heuristic approaches.

In this work, we apply a similar strategy where we identify structural features based on our understanding of fast Li-ion motion and use these features in a large-scale search for new lithium oxide SICs and new structural frameworks. We start by revisiting the ion-conduction mechanisms in lithium garnet and NASICON structures, and identify a 3D percolation Li diffusion network and a moving “activated local environment” as crucial factors for achieving superionic conduction. By translating these factors into three structural features we were able to perform a high-throughput screening across the Inorganic Crystal Structure Database (ICSD)<sup>[49]</sup> to identify structures with a network of Li sites that is amenable to fast Li-ion motion. The ionic conductivity of promising structures was evaluated in more detail using ab initio molecular dynamics (AIMD) simulations. From this search, we identify 7 promising lithium oxide SIC candidates with high room-temperature ionic conductivity. Their structural frameworks such as spinel, oxy-argyrodite, sodalite, and  $\text{LiM}(\text{SeO}_3)_2$  open up new

opportunities for enriching the structural families of lithium oxide SICs.

## 2. Results

### 2.1. Li Diffusion Networks in Garnet and NASICON Structures

To achieve high ionic conductivity in a material, Li ions need to migrate between Li sites with low activation energy. Here, we define the Li diffusion network as a graph of face-sharing Li sites in the crystal structure of a material. A possible Li site is defined as the center of a polyhedron formed by  $\text{O}^{2-}$  anion corners and is represented by a node in the network, and a “face” is defined as an  $\text{O}^{2-}$  triangular facet of a polyhedron. The face-sharing relation between two Li sites is represented by an edge between corresponding nodes in the network. Thus, the Li diffusion network can be viewed as a road map for Li-ion transport in the material. For example, **Figure 1A,D** shows the crystal structures of  $\text{Li}_3$  garnet ( $\text{Li}_3\text{La}_3\text{Te}_2\text{O}_{12}$ ) and pristine NASICON ( $\text{LiTi}_2(\text{PO}_4)_3$ ), respectively. Simplified 2D representations of their Li diffusion networks are presented in **Figure 1B,E**, respectively. For clarity, Li sites not participating in the ion conduction are not displayed in the network.

Garnets are known to have a framework that is beneficial for Li-ion conduction.<sup>[41,50–53]</sup> The Li diffusion network of garnets is 3D, and every two neighboring tetrahedral (tet) 24d sites are bridged by an intermediate octahedral (oct) 48g/96h site<sup>[8,54]</sup>

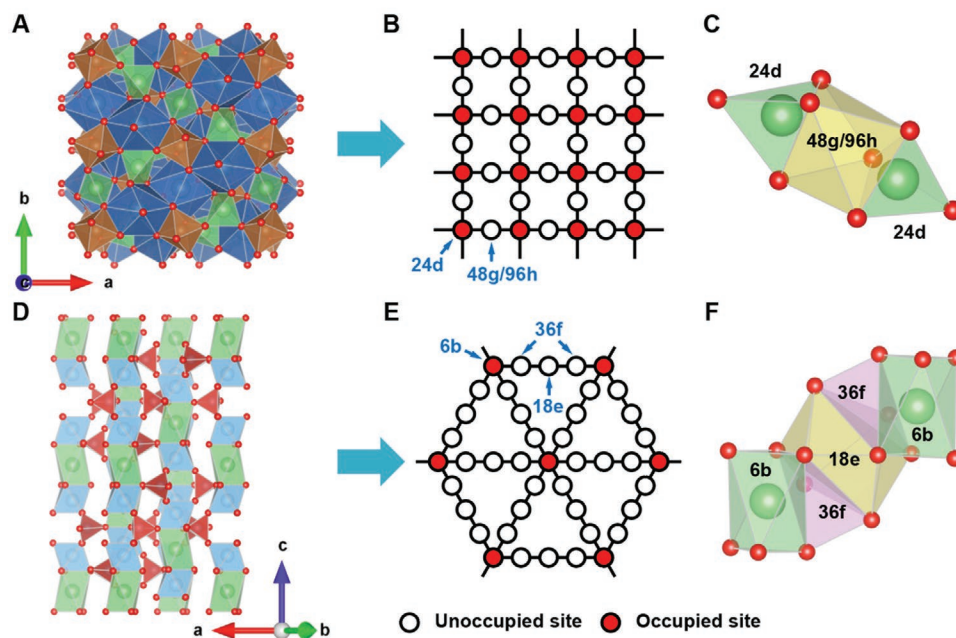


**Figure 1.** Crystal structures, 2D representations of Li diffusion networks, and local environments of  $\text{Li}_3$  garnet and pristine NASICON. A–C) Crystal structure of  $\text{Li}_3$  garnet with the composition  $\text{Li}_3\text{La}_3\text{Te}_2\text{O}_{12}$  (A) and simplified 2D representation of its Li diffusion network (B). The site arrangement in the local environment between neighboring 24d sites is shown in (C). Green tetrahedrons: Li 24d sites, yellow octahedrons: Li 48g/96h sites, brown octahedrons:  $\text{TeO}_6$ , blue polyhedrons:  $\text{LaO}_8$ . D–F) Crystal structure of NASICON with the composition  $\text{LiTi}_2(\text{PO}_4)_3$  (D) and simplified 2D representation of its Li diffusion network (E). The site arrangement in the local environment between neighboring 6b sites is shown in (F). Green octahedrons: Li 6b sites, yellow polyhedrons: Li 18e sites, purple tetrahedrons: Li 36f sites, red tetrahedrons:  $\text{PO}_4$ , blue octahedrons:  $\text{TiO}_6$ . Green spheres: Li-ions, red spheres:  $\text{O}^{2-}$  anions. Each circle in the Li diffusion network represents a Li site. An edge between two circles exists if their corresponding sites are face-sharing with each other. Empty circles: unoccupied Li sites, solid red circles: occupied Li sites.



(Figure 1B). As a result, each percolation transport path in the garnet framework has the –tet–oct–tet–oct– site configuration. In a Li<sub>3</sub> garnet such as Li<sub>3</sub>La<sub>3</sub>Te<sub>2</sub>O<sub>12</sub>, only the tetrahedral 24d sites are fully occupied by Li ions, whereas the octahedral 48g/96h sites are vacant<sup>[52]</sup> (Figure 1B). We define a local environment as the path between two neighboring occupied Li-sites in the pristine structure. Notably, all local environments of the path between two neighboring 24d sites are symmetrically equivalent. Therefore, a Li transport path in the Li<sub>3</sub> garnet network is composed of the same local environment between neighboring occupied Li-ions, which we describe as the “homogeneity” of the transport path (refer to Section “Quantification of network features” for precise definitions). The specific site arrangement of this local environment is shown in Figure 1C.

The Li diffusion network of NASICONs is topologically similar to that of the Li<sub>3</sub> garnet in three ways: 1) the network is also 3D;<sup>[55]</sup> 2) only the crossing nodes (octahedral 6b sites) in the network are occupied for the pristine composition (Figure 1E),<sup>[55]</sup> and 3) the transport path in the network also has homogeneity as shown in Figure 1E, where the specific site arrangement of the local environment between neighboring occupied 6b sites is shown in Figure 1F. These shared topological similarities between garnet and NASICON networks suggest a common pattern in their ion-conduction mechanisms, which will be

discussed in the next section. However, one significant difference between the two networks is that the distance between occupied crossing nodes is much larger in the pristine NASICON (6.02 Å) than that in the Li<sub>3</sub> garnet (3.94 Å). The difference exists because there are three intermediate bridging nodes (36f, 18e, 36f) between crossing nodes in the NASICON (Figure 1F),<sup>[55]</sup> whereas in the Li<sub>3</sub> garnet, there is only one (Figure 1C).

## 2.2. Ion-Conduction Mechanisms in Garnet and NASICON Frameworks

The ion-conduction mechanisms in garnet and NASICON frameworks have been extensively studied both computationally and experimentally,<sup>[41,42,52,55,56]</sup> and can be illustrated with the Li diffusion network<sup>[41,52]</sup> as shown in Figure 2.

The lithium garnet Li<sub>x</sub>A<sub>3</sub>B<sub>2</sub>O<sub>12</sub> (denoted as “Lix garnet”) has a robust framework that can accommodate a wide range of Li concentrations ( $x = 3-7$ , or Li<sub>3</sub>–Li<sub>7</sub>).<sup>[8,50]</sup> Experimentally, even a slight increase of  $x$  from 3 to 3.1 leads to a steep increase of ionic conductivity of 3 orders of magnitude at 400 °C.<sup>[57]</sup> As  $x$  further increases toward 7, the room-temperature conductivity approaches  $\approx 10^{-4}$  S cm<sup>-1</sup>,<sup>[8,58]</sup> with a peak value of approximately  $10^{-3}$  S cm<sup>-1</sup> achieved at  $x = 6.4$ <sup>[8,59]</sup> or 6.7.<sup>[60]</sup> Previous

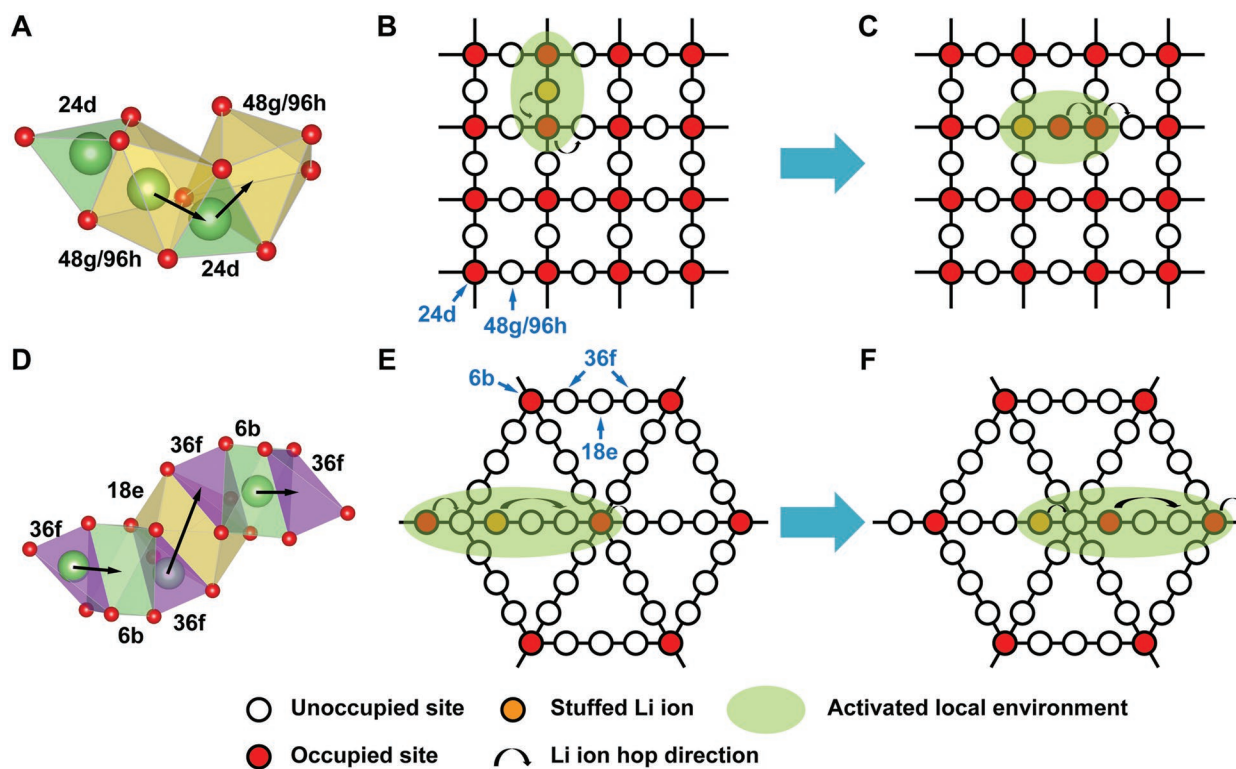


**Figure 2.** Li-ion conduction in Li-stuffed Li<sub>3</sub> garnet and NASICON via cooperative hopping of Li ions in “activated local environment.” A–C) Cooperative hopping of two Li ions in 24d and 48g/96h sites in the Li-stuffed garnet framework illustrated in the local environment (A) and in the simplified 2D Li diffusion network (B). The Li diffusion network after one step of cooperative hopping is shown in (C). Green tetrahedrons: Li 24d sites, yellow octahedrons: Li 48g/96h sites. D–F) Cooperative hopping of three Li ions in 36f, 36f, and 6b sites in the Li-stuffed NASICON framework illustrated in the local environment (D) and in the simplified 2D Li diffusion network (E). The Li diffusion network after one step of cooperative hopping is shown in (F). Green octahedrons: Li 6b sites, yellow polyhedrons: Li 18e sites, purple tetrahedrons: Li 36f sites. Empty circles: unoccupied Li sites, solid red circles: occupied Li sites, solid orange circles: sites occupied by the stuffed Li-ions. Green ellipse: the activated local environment, arrows: the next hopping directions of Li ions.

computational studies have mostly focused on the ion-conduction mechanism of garnets with  $x$  near 7.<sup>[41,42,52]</sup> At such a high Li concentration, AIMD simulation results have suggested that the low activation energy of approximately 300 meV can be attributed to the cooperative motion of Li ions in the face-sharing tetrahedral 24d sites and octahedral 48g/96h sites resulting from the strong coulombic interaction between them.<sup>[41,42]</sup>

In contrast, the ionic conduction mechanism of garnets at  $x = 3 + \delta$  has been computationally less explored, despite the “switching-on” of the fast ionic conduction behavior at this composition.<sup>[8,56,57]</sup> In a pristine Li<sub>3</sub> garnet, Li-ion migration involves moving a tetrahedral Li-ion to a neighboring octahedral site with a barrier greater than 1 eV,<sup>[43,52,57]</sup> explaining its negligible conductivity at room temperature. As a dilute amount of Li ions is stuffed into the Li<sub>3</sub> garnet to reach  $x = 3 + 1/8$ , density functional theory (DFT) results show that the stuffed Li-ion resides in the octahedral 48g/96h site, creating a local tet–oct–tet Li-ion arrangement, as shown in Figure 2A and the green shaded area in Figure 2B. The short Li<sup>+</sup>–Li<sup>+</sup> distance of 2.27 Å between the face-sharing tetrahedral and octahedral Li-ions induces strong coulombic repulsion similar to that in the Li<sub>7</sub> case,<sup>[41,42]</sup> suggesting that coordinated motion may also occur in the Li<sub>3</sub>+ $\delta$  garnets. Migration of Li occurs when the stuffed octahedral Li-ion moves to a face-sharing tetrahedral site and pushes the Li-ion originally at that site to another octahedral site, as illustrated in Figure 2A,B. Indeed, an activation energy of only 160 meV is calculated using the nudged elastic band (NEB) method for this mechanism (Figure S1, Supporting Information); this low NEB barrier is further supported by a similar activation energy of  $198 \pm 84$  meV determined from AIMD simulation (Figure S2, Supporting Information).

From the abstract viewpoint of the Li diffusion network, the conduction mechanism of the NASICON-structured Li<sub>1-x</sub>Al<sub>x</sub>Ti<sub>2-x</sub>(PO<sub>4</sub>)<sub>3</sub> is similar to that of Li<sub>3</sub>+ $\delta$  garnet,<sup>[55]</sup> which can be attributed to the similarities in their network topology. Indeed, upon Li stuffing, the measured bulk ionic conductivity of the NASICON is enhanced by a factor of 3–30<sup>[61–64]</sup> with a reduction of the activation energy by 70–160 meV.<sup>[63,65]</sup> As the Li content in NASICON increases above LiM<sub>2</sub>(PO<sub>4</sub>)<sub>3</sub>, both experimental and DFT results indicate that the extra Li resides in the tetrahedral 36f site and displaces the face-sharing octahedral 6b Li-ion to the opposite tetrahedral 36f site, leaving a distance of 3.25 Å between them (Figure 2D).<sup>[55,66,67]</sup> As reported by Lang et al.,<sup>[55]</sup> the interstitial ion conduction involves a cooperative hopping of three Li-ions, 2 in 36f sites and one in 6b site, as illustrated in Figure 2D,E. Specifically, in the NASICON network, two Li ions in 36f sites marked in the green shaded area in Figure 2E hop right to the octahedral 6b and tetrahedral 36f sites. At the same time, the octahedral 6b Li-ion originally in the center of the network is pushed to the tetrahedral 36f site on the right.<sup>[55]</sup> The NEB barrier of 190 meV for this mechanism as calculated by Lang et al.<sup>[55]</sup> is supported by our AIMD result which finds very similar activation energy of  $186 \pm 47$  meV (Figure S3, Supporting Information).

Notably, at the end of both cooperative motions in the garnet and NASICON networks, a new local environment containing an interstitial Li-ion is created, as indicated by the green shaded areas in Figure 2C,F. Because both pristine networks have homogenous transport paths, the green shaded local environments in Figure 2C,F are symmetrically equivalent to those in

Figure 2B,E, and can continue to propagate in the network via the exact same cooperative hopping mechanism.

### 2.3. Screening Strategies of Lithium Oxide SICs

There is a common pattern in the ion-conduction mechanism of the Li-stuffed garnet and NASICON framework. In each compound, the local environments in the pristine network are quiescent for ionic conduction. Stuffing an excess Li-ion into the pristine network creates an “activated” local environment where the migration barrier of Li ions is much lower via cooperative motion. The activated local environment can then propagate in the diffusion network, leading to percolation, as demonstrated in Figure 2. We will refer to this as an “activated diffusion network.” This pattern can also be applied to other Li-ion conductors with a cooperative motion or “kick-out” mechanism such as Li<sub>1-2x</sub>Zn<sub>1-x</sub>PS<sub>4</sub><sup>[27]</sup> or Li<sub>3</sub>PO<sub>4</sub>.<sup>[68]</sup> The pattern also suggests a physical picture where only the activated local environments contribute to the ionic conduction while the rest of the network remains quiescent, a mechanism that has also been suggested for ionic migration in glass systems.<sup>[69–71]</sup> We note that while a simple interstitialcy mechanism does not give us any information on which structures can be fast ionic conductors after stuffing an excess Li-ion, our proposed concept of “activated diffusion network” provides a more specific physical picture regarding what is the nature of the defects that induces fast Li-ion motion and which structures can accommodate them.

For compounds with this pattern to become fast Li-ion conductors, two additional requirements need to be met: 1) initiation of the activation, meaning that it has to be possible for the stuffed Li to create the activated local environment in the network, and 2) propagation of the activation, meaning that the activation is able to keep propagating in the network without dying out (i.e., the interstitial Li-ion will not be trapped in a local environment where there is an energy basin) and will eventually percolate throughout the network.

These requirements can be met in the garnet and NASICON framework. Both the garnet and NASICON frameworks have a 3D percolation network which allows the activation to propagate in all three dimensions, limiting the effect that diffusion is blocked by point defects as is the case for 1D diffusion.<sup>[72]</sup> Therefore, the 3D feature is beneficial for the propagation of activation (requirement 2).

The pristine networks of both Li<sub>3</sub> garnet and NASICON also have homogenous transport paths. This feature guarantees that once activation is initiated in the network, it will not die out during the propagation, as any local environment to which the interstitial Li-ion moves will be equivalent to the first activated local environment, as observed in Figure 2C,F. This feature is thus also beneficial for the propagation of activation (requirement 2).

Finally, the distances between all neighboring occupied Li sites are short in Li<sub>3</sub> garnet. This feature is only present in the network of the Li<sub>3</sub> garnet but not in that of the NASICON. Specifically, the cartesian distance between two neighboring occupied tetrahedral 24d sites is only 3.94 Å in Li<sub>3</sub> garnet. After Li stuffing, the stuffed Li-ion is inserted into the middle of two 24d Li-ions, cutting the local Li<sup>+</sup>–Li<sup>+</sup> distance by half to

1.97 Å before structural relaxation and to 2.27 Å after relaxation. Such a short  $\text{Li}^+-\text{Li}^+$  distance can result in a strong coulombic interaction in the local environment and likely contributes to a lowered Li hopping barrier,<sup>[42]</sup> that is, the initiation of activation (requirement 1). The same effect also applies to the propagation process, as any local environment to which the interstitial Li-ion moves will also likely be activated owing to the short distance between occupied Li sites there. This feature is thus beneficial for both requirements 1 and 2.

In comparison, the distance between occupied 6b sites in the NASICON network is much larger (6.02 Å). After Li stuffing, the shortest  $\text{Li}^+-\text{Li}^+$  distance becomes 3.25 Å after relaxation, which is 1-Å larger than that in the Li-stuffed Li3 garnet (2.27 Å), corresponding to a much weaker Coulomb force between nearest Li-ions. Therefore, the initiation of the activation in the Li-stuffed NASICON network may not simply be caused by the local coulombic interactions and should also be attributed to the relatively flat energy landscape of the NASICON structure. Indeed, AIMD results reveal that Li ions in the Li3 garnet are much more localized in its equilibrium 24d sites than in the pristine NASICON, as indicated by their mean square displacements (Figure S4, Supporting Information). As a result, we end up with two beneficial network features for the NASICON network: a 3D network and homogeneity of the transport path. For the Li3 garnet network, there is an additional feature: the short distances between occupied Li sites.

Inspired by the common ion-conduction pattern and network features in garnets and NASICONs, we have proposed two strategies for identifying new garnet-like and NASICON-like Li oxide SICs using two different combinations of features.

Potential garnet-like SICs include compounds with 1) a 3D percolating lithium diffusion network and 2) a short distance of  $\leq 4$  Å between all neighboring occupied Li sites along the transport path of the pristine network. The value of 4 Å is referenced to that in Li3 garnet (3.94 Å), such that after Li stuffing, the shortest  $\text{Li}^+-\text{Li}^+$  distance will be below 2 Å, creating a similar or even stronger local coulombic interaction than that in the Li-stuffed Li3 garnet. This combination of features will benefit both the initiation (requirement 1) and propagation (requirement 2) of the activation. Therefore, the homogeneity of the transport path is not a necessity, although it is also present in the Li3 garnet network.

Potential NASICON-like SICs include compounds with 1) a 3D percolating lithium diffusion network and 2) homogeneity of the transport path in the pristine network. This combination of features will only benefit the propagation of the activation (requirement 2). Whether this activation can be initiated upon Li stuffing (requirement 1) still depends on the specific framework. In the next section, we describe how these features are defined and computed so that they can be applied to a high-throughput search for new Li-ion conducting oxides.

## 2.4. Quantification of Network Features

To find the Li diffusion network and percolation dimensionality we performed Delaunay tetrahedralization<sup>[73,74]</sup> on the crystal framework to find all potential Li sites, which are then represented as individual nodes in the Li diffusion network graph. Nodes that correspond to partially or fully occupied Li sites

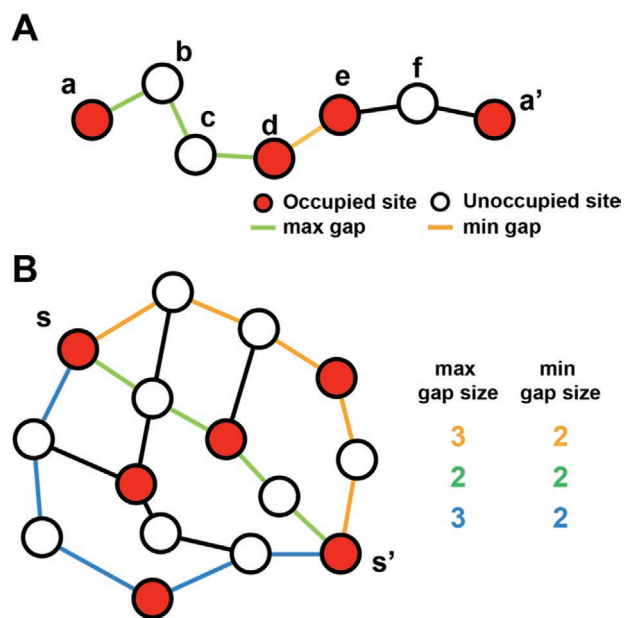


**Figure 3.** Schematic example of transport paths and the definition of “gap.” A) An example transport path from a Li site  $a$  to its periodic image  $a'$  through face-sharing Li sites (circles). Each edge has a length of 1. The max gap consists of green edges between sites  $a$  and  $d$  with a gap size of 3. The min gap consists of the orange edge between sites  $d$  and  $e$  with a gap size of 1. B) An example Li diffusion network between a Li site  $s$  and its periodic image  $s'$ . Three example transport paths from  $s$  to  $s'$  are colored in orange, green, and blue. Each edge has a length of 1. The max and min gap size for each transport path are summarized in the inset table. The green path with the smallest max gap size is selected as the “representative transport path” in the network.

are denoted as “occupied nodes,” and the rest are denoted as “unoccupied nodes.” Edges are drawn between two nodes if their corresponding sites are face-sharing with each other. The dimensionality of the network is defined as the number of dimensions in which at least one occupied node can percolate to its next periodic image. More details on the construction of the Li diffusion network and percolation analysis are provided in Note S1, Supporting Information.

### 2.4.1. Gap and Gap Size

We defined the “gap” as the pathway between two neighboring occupied Li sites connected by a series of face-sharing unoccupied Li sites. Therefore, the gap is a suitable representation of the local environment in the network. In the example transport path in Figure 3A, there are three gaps 1)  $a-b-c-d$ , 2)  $d-e$ , and 3)  $e-f-a'$ . In this work, we use “gap size,” which is the total length of the gap, to represent the distance between occupied Li sites. Assuming all the edges have a length of 1 in Figure 3A, the three gap sizes are 3, 1, and 2, respectively. The advantage of using gap size instead of cartesian distance will be explained later.

### 2.4.2. Maximum and Minimum Gap Size

We define “transport path” as the 1D path consisting of a series of gaps (or local environments) that connect a Li-site to its

periodic image. Each transport path in the diffusion network is composed of multiple gaps, such as those in Figure 3A. Two key quantities are recorded: the maximum (max) and minimum (min) gap size. For example, for the transport path in Figure 3A, the max gap size is 3 and the min gap size is 1. To find garnet-like SICs, we replace the second requirement on the site distances with a new requirement that the “max gap size of the transport path in the pristine network must be  $\leq 4$  Å.” For a pristine network meeting this requirement, the min gap size of the transport path containing an extra stuffed Li will be equal to or less than 2 Å (neglecting relaxation). The strong coulombic interaction that will be present when Li is stuffed in such a gap can initiate the activation as in the Li<sub>3</sub> garnet. We note that this convenient property of the gap size does not hold for cartesian distance because the stuffed Li-ion may not be positioned precisely on the line segment between two occupied Li sites. Instead, the gap size measures the cumulative distance traveled as an ion moves through sites.

#### 2.4.3. Homogeneity of the Transport Path

In a strict sense, the condition “homogeneity of the transport path” requires all gaps in a Li-ion transport path to be symmetrically equivalent local environments. Figure S5, Supporting Information, provides a comparison between 1D examples of homogeneous and inhomogeneous transport paths. In this work, we used a weaker condition requiring that the max gap size is equal to the min gap size in the transport path of the pristine network. This weaker condition guarantees that all gaps in the transport path have the same size, which is a strong indication of the strict equivalence of all gaps. Using the max gap size in the pristine NASICON network (6.73 Å) as a reference, we focus on compounds with a max gap size  $\leq 7$  Å in this work.

#### 2.4.4. Representative Transport Path

Several percolation transport paths often exist in a Li diffusion network, some of which consist of high-energy sites that are not involved in Li-ion conduction. In this work, only the transport path with the smallest max gap size was selected as the “representative transport path” for the gap size analysis of the network. For example, from the three transport paths in Figure 3B between a node *s* and its periodic image node *s'*, the green path will be selected. This set of assumptions will lead to finding the actual ion transport paths for garnet and NASICON structures. More details on the path selection are provided in Note S1, Supporting Information. We note that our selection of the representative transport path may lead to underestimation of the max gap size of the actual transport path in some materials, and therefore may include some bad conductors during the screening process, but these false positives will eventually be filtered out using AIMD simulation in the later screening steps.

With the network features defined as computable quantities, we formally translate the two strategies for finding garnet-like and NASICON-like SICs into two regimes. The requirements

for the garnet regime are 1) percolation dimensionality = 3 and 2) max gap size  $\leq 4$  Å for the pristine Li diffusion network. The requirements for the NASICON regime are 1) percolation dimensionality = 3 and 2)  $4 \text{ Å} < \text{min gap size} = \text{max gap size} \leq 7 \text{ Å}$  for the pristine Li diffusion network. Note that we do not consider min gap size  $\leq 4$  Å in the NASICON regime as this would overlap with the garnet regime. We then perform a high-throughput screening of structures from the ICSD to search for new lithium oxide SICs.

### 2.5. High-Throughput Screening

The screening procedure to find potential lithium oxide SICs is described in Figure 4. Starting with 6242 Li-containing oxides with at least three elements from the ICSD,<sup>[49]</sup> we constructed for each compound the Li diffusion network and analyzed its percolation dimensionality. At this step, invalid structures (e.g., invalid cif files, missing Li, unfit for Delaunay tetrahedralization, etc.) were excluded, and only Li diffusion networks with percolation dimensionality of 3 were selected.

For the remaining 4666 oxides, the min and max gap sizes of the representative transport path were computed, the results of which are shown in Figure 5. This min-max gap size plot provides direct visualization of the garnet regime (orange shaded triangle) and the NASICON regime (blue shaded ellipse). There are 1479 oxides in the garnet regime and 361 oxides in the NASICON regime for a total of 1840 oxides.

Intriguingly, although the garnet and NASICON regimes were defined using features from the Li<sub>3</sub> garnet (red star) and NASICON (yellow star) networks, three other well-known lithium oxide SICs fall into these two regimes, namely, perovskite (green star), antiperovskite (pink star), and LISICON (blue star), as shown in Figure 5. Of these five oxide SICs, four have a max gap size  $\leq 4$  Å, four have the homogeneity of the transport path (the diagonal line), and all of them have a 3D diffusion network. This result is encouraging, as it suggests that the beneficial structural features we extracted from garnet and NASICON networks are likely shared by a large portion of lithium oxide SICs.

The 1840 compounds passing the min-max gap size analysis were further grouped into 243 groups (157 for the garnet regime and 86 for the NASICON regime) based on the similarity of their framework structures using the Structure Matcher in the pymatgen software package.<sup>[75]</sup> Because compounds within the same structural group should in principle have similar Li diffusion networks, we only selected one structure from each group for the subsequent screening procedures. The focus on structure topology rather than specific cation chemistry is reasonable since for many lithium SICs such as the garnet,<sup>[8,31]</sup> NASICON,<sup>[2,9]</sup> and (thio)-LISICON families<sup>[2,76]</sup> the non-Li cations can be selected from a wide range of elements. Once a good conductor is identified, the other compounds in the structure group can always be reinvestigated to achieve further optimization of conductivity or other desired properties.

When selecting the one representative structure from each group, we excluded the following compounds: 1) Compounds in which all available vacant sites face-share with multiple cations, likely preventing Li stuffing of the structure. For typical vacant



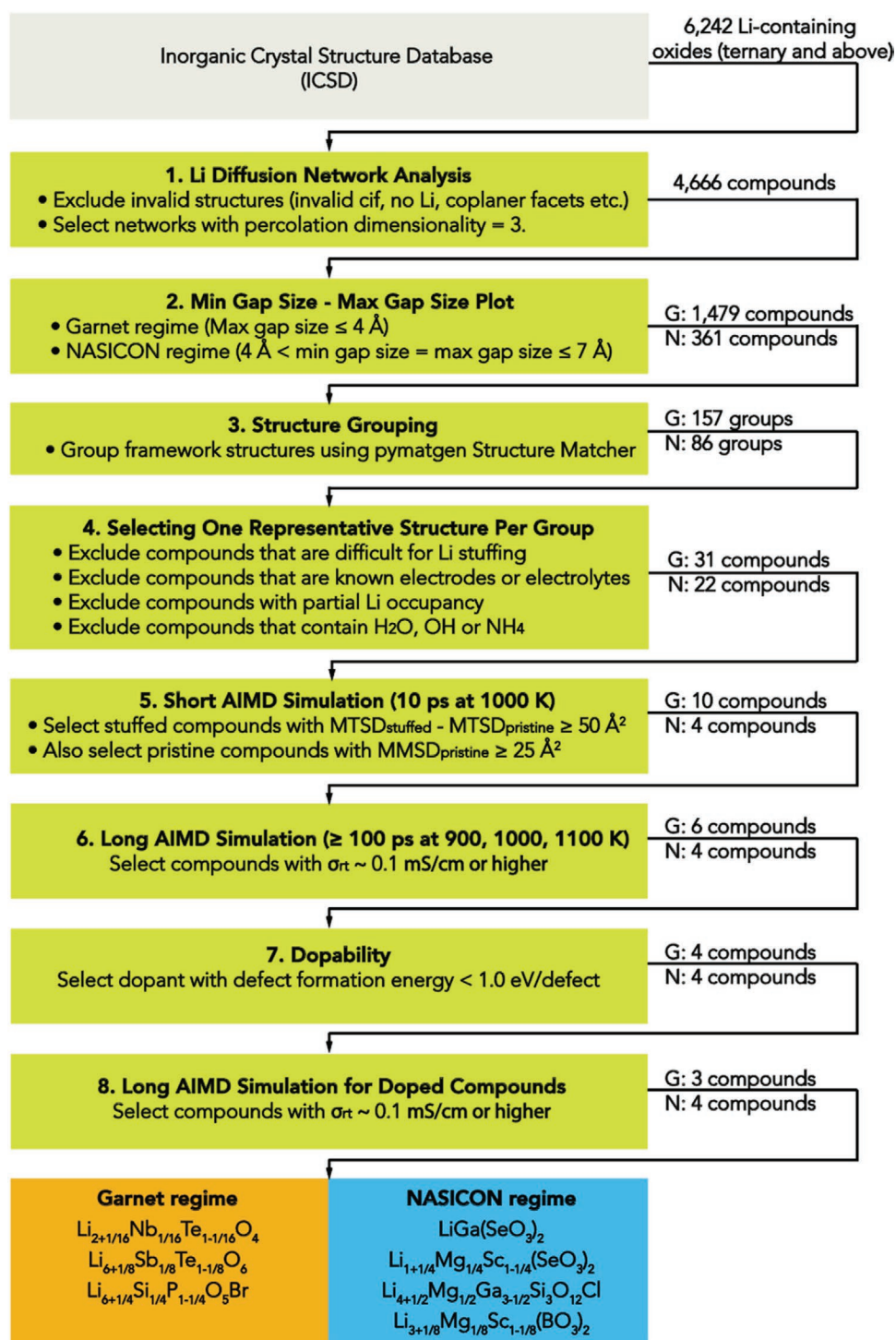


**Figure 4.** Flowchart describing the computational screening procedures for lithium oxide SICs. MTSD is the maximum total square displacement, MMSD is the maximum mean square displacement, and σ<sub>rt</sub> is the extrapolated room-temperature conductivity from AIMD simulations. G and N represent the garnet and NASICON regimes, respectively.

tetrahedral and octahedral sites, we limited the maximum number of face-sharing cations to 2 and 4, respectively (half the number of their polyhedron faces). For example, LiInO<sub>2</sub> (ICSD ID: 44 522) has an fcc anion framework where all octahedral sites are occupied by cations. This compound was excluded as

every vacant tetrahedral site face-shares with four other cations. 2) Compounds already investigated for lithium electrode or electrolyte applications, including lithium garnets, NASICONs, perovskites, antiperovskites, and electrode materials with redox elements such as Li<sub>2</sub>VPO<sub>4</sub>F (ICSD ID: 183 877). 3) Compounds



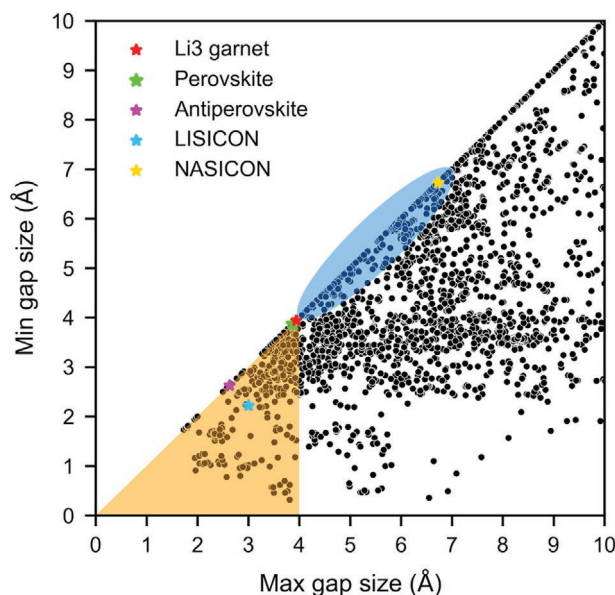


**Figure 5.** Classification of Li diffusion networks using the min and max gap size analysis. Plot of min gap size vs. max gap size for 4666 lithium oxides from the Li diffusion network analysis (filter 1). The garnet regime (max gap size  $\leq 4$  Å) is shaded orange, and the NASICON regime ( $4$  Å  $<$  min gap size = max gap size  $\leq 7$  Å) is shaded blue. Note that the ellipse shown for the NASICON regime is only provided as a visual aid; the actual NASICON regime is only the segment along the diagonal. Red star: Li<sub>3</sub> garnet ( $\text{Li}_3\text{La}_3(\text{TeO}_6)_2$ ), green star: perovskite ( $\text{Li}_{0.33}\text{La}_{0.557}\text{TiO}_3$ ), pink star: antiperovskite ( $\text{Li}_3\text{OCl}$ ), blue star: LISICON ( $\text{Li}_{14}\text{Zn}(\text{GeO}_4)_4$ ), yellow star: NASICON ( $\text{LiTi}_2(\text{PO}_4)_3$ ). See also Table S1, Supporting Information, for the max and min gap size values of the stars.

with disordered Li sites. These compounds often require a computationally expensive investigation of the Li configurational thermodynamics. Moreover, if the disordered Li sites contain non-Li cations, these non-Li cations may block the Li transport paths. This criterion does not exclude potential fast Li-ion conductors with Li-site disorder, as most SICs were engineered from an originally ordered material such as Li-3 garnet or stoichiometric Li-1 NASICON. We note that if the disordered compound from the ICSD database has an ordered structure found in the Materials Project database<sup>[77]</sup> or our internal database of DFT-computed structures, we would use that ordered structure for later analysis. 4) Compounds that contain  $\text{H}_2\text{O}$ ,  $\text{OH}$ , or  $\text{NH}_4$ . Cif files of these compounds often have missing proton coordinates, and they may also lose  $\text{H}_2\text{O}$  or  $\text{NH}_3$  during the high-temperature processing. If all compounds in a structure group were excluded, then that group was abandoned.

After this step, 31 compounds remain in the garnet regime and 22 compounds remain in the NASICON regime. Their specific compositions and ICSD IDs are listed in Tables S2 and S3, Supporting Information, respectively.

We evaluated the ionic conductivity of these 53 compounds with and without Li stuffing using AIMD simulations. However, performing AIMD simulations for all 53 compounds at multiple temperatures and for a long simulation time ( $\geq 100$  ps) would be computationally very expensive. Instead, for each compound, we performed short AIMD simulations for 10 ps at 1000K for both the pristine and Li-stuffed compositions to

detect signs of drastically improved conductivity upon Li stuffing. If a local environment in the pristine structure can indeed be activated by the stuffed Li ion, a drastic increase is expected in the maximum total square displacement (MTSD) of Li ions obtained from the short AIMD simulation after Li stuffing. The MTSD is defined as:

$$\text{MTSD} = \max_{0 \text{ ps} \leq t \leq 10 \text{ ps}} \sum_{i=1}^N |\mathbf{r}_i(t)|^2 \quad (1)$$

Here,  $N$  is the number of Li ions,  $t$  is a variable between 0 and 10 ps,  $i$  is the index of the Li-ion, and  $\mathbf{r}_i(t)$  is the displacement vector of the Li-ion  $i$  at time  $t$  with respect to its initial position  $\mathbf{r}_i(t=0)$ .

As noted earlier, the “activated diffusion network” model assumes that only the activated local environment contributes to the Li-ion diffusion and that the rest of the networks remain quiescent; therefore, the difference between the MTSD of the stuffed and pristine material ( $\text{MTSD}_{\text{stuffed}} - \text{MTSD}_{\text{pristine}}$ ) reflects only the contribution of the activated local environment to the MTSD. As a reference,  $\text{MTSD}_{\text{stuffed}} - \text{MTSD}_{\text{pristine}}$  is  $64 \text{ Å}^2$  for Li<sub>3</sub> garnet and  $106 \text{ Å}^2$  for NASICON over a 10-ps AIMD simulation, and we therefore set the threshold for  $\text{MTSD}_{\text{stuffed}} - \text{MTSD}_{\text{pristine}}$  at  $50 \text{ Å}^2$ . Conceptually, this threshold value is roughly equivalent to one Li-ion migrating over 7 Å or two Li-ions each migrating over 5 Å within 10 ps. **Figure 6** plots the MTSD of the Li-stuffed structure ( $\text{MTSD}_{\text{stuffed}}$ ) vs. that of the pristine structure ( $\text{MTSD}_{\text{pristine}}$ ) for the 53 compounds passing filter 4 in the screening. The contour line where  $\text{MTSD}_{\text{stuffed}} - \text{MTSD}_{\text{pristine}} = 50 \text{ Å}^2$  is highlighted in green. The 10 stuffed compounds in the

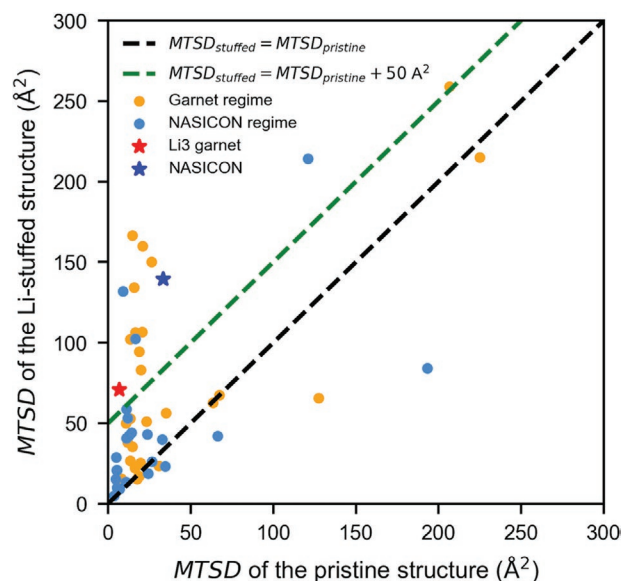


**Figure 6.** Short AIMD simulation results for 53 compounds. MTSD of the stuffed compound ( $\text{MTSD}_{\text{stuffed}}$ ) vs. MTSD of the pristine compound ( $\text{MTSD}_{\text{pristine}}$ ) for 53 compounds over 10-ps short AIMD simulation (Filter 5). The orange and blue points represent compounds from the garnet and NASICON regimes, respectively. Red star: Li<sub>3</sub> garnet ( $\text{Li}_3\text{La}_3\text{Te}_2\text{O}_{12}$ ), blue star: NASICON ( $\text{LiTi}_2(\text{PO}_4)_3$ ). Black dashed line:  $\text{MTSD}_{\text{stuffed}} = \text{MTSD}_{\text{pristine}}$ , green dashed line:  $\text{MTSD}_{\text{stuffed}} = \text{MTSD}_{\text{pristine}} + 50 \text{ Å}^2$ . Points above the green dashed line were passed to filter 6 for long AIMD simulations.

garnet regime and the 3 stuffed compounds in the NASICON regime above the green line pass the short AIMD filter. Table 1 summarizes their compositional information, ICSD IDs, and computed properties.

In addition to compounds showing signs of improved ionic conductivity only after Li stuffing, the short AIMD simulation also identified the NASICON-regime compound  $\text{LiGa}(\text{SeO}_3)_2$  with a high maximum mean square displacement (MMSD)  $\geq 25 \text{ \AA}^2$  even for the pristine composition, where MMSD is defined as  $\text{MMSD} = \text{MTSD}/N$ . This compound may already exhibit high ionic conductivity in its pristine form and was thus also included as a candidate for lithium SICs in Table 1. In total, 10 compounds in the garnet regime and 4 compounds in the NASICON regime pass the short-AIMD filter. The MTSD and MMSD values of all 53 compounds from the short AIMD simulations are also provided in Tables S2 and S3, Supporting Information.

In the next filter (Filter 6), we ran long AIMD simulations for at least 100 ps and at least three temperatures (900 K, 1000 K, and 1100 K) for all 14 compounds. Their extrapolated room-temperature conductivities ( $\sigma_{\text{rt, stuffed}}$ ) and activation energies ( $E_{\text{a, stuffed}}$ ) are summarized in Table 1. Four compounds in the garnet regime had  $\sigma_{\text{rt, stuffed}}$  lower than  $0.1 \text{ mS cm}^{-1}$  and were filtered out at this step. As a result, 9 Li-stuffed compounds (6 for the garnet regime and 3 for the NASICON regime) were passed to the next filter to estimate their dopability. The compound  $\text{LiGa}(\text{SeO}_3)_2$  with  $\sigma_{\text{rt}}$  of  $0.21 \text{ mS cm}^{-1}$  was added directly to the final list of lithium SIC candidates as no further doping is needed.

The Li-stuffed compounds require subvalent doping on the non-Li sites for charge compensation. However, stuffing Li ions into high-energy sites and substituting elements in the pristine compound may destabilize the structure, as indicated by the positive defect formation energies ( $E_{\text{defect}}$ ) for doping in known SICs.<sup>[78,79]</sup> For example, we calculated the defect formation energy for the substitution of a  $\text{Zn}^{2+}$  ion by two  $\text{Li}^+$  ions in  $\text{LiZnPS}_4$  to be  $0.34 \text{ eV/defect}$ , and that for the substitution of  $\text{Ti}^{4+}$  by  $\text{Al}^{3+}$  and  $\text{Li}^+$  in  $\text{LiTi}(\text{PO}_4)_3$  NASICON to be  $0.40 \text{ eV/defect}$ . Because a large  $E_{\text{defect}}$  value suggests poor dopability of the pristine compound and thus poor synthesizability of the stuffed composition, it is important to select a dopant with a low defect formation energy. For each of the 9 compounds that required Li stuffing, we tested dopant ions with a high substitution correlation ( $>1$ ) as identified in the previous data mining work<sup>[80]</sup> or a small difference ( $<0.15 \text{ \AA}$ ) in Shannon radius with the ion to be replaced. For each compound, the dopant with the lowest defect formation energy is listed in Table 1. The energy above the hull ( $E_{\text{above hull}}$ ) values for the doped structures are also listed for reference. We set the criterion for good dopability to be  $E_{\text{defect}} < 1 \text{ eV/defect}$ , a threshold much higher than that of Al-doped  $\text{LiTi}_2(\text{PO}_4)_3$  ( $0.40 \text{ eV/defect}$ ) and Li-doped  $\text{LiZnPS}_4$  ( $0.34 \text{ eV/defect}$ ). This criterion filtered out  $\text{Li}_4\text{SiO}_4$  and  $\text{Li}_2\text{MgPO}_4\text{F}$  from the garnet regime for which the lowest defect formation energies we could find were  $1.52$  and  $1.33 \text{ eV/defect}$ , respectively. Intriguingly, although most of the compounds in Table 1 have varying  $E_{\text{defect}}$  from  $0.5$  to  $0.8 \text{ eV/defect}$ , the compound  $\text{LiSc}(\text{SeO}_3)_2$  has an  $E_{\text{defect}}$  of  $0 \text{ eV/defect}$  by doping Sc with Mg, indicating that this material is thermodynamically stable even after Li-stuffing.

For the last filter (Filter 8), we ran long AIMD simulations for at least five temperatures between 800 and 1200 K for the 7 doped structures (4 in the garnet regime and 3 in the NASICON regime). Their extrapolated room-temperature ionic conductivities ( $\sigma_{\text{rt, doped}}$ ) and activation energies ( $E_{\text{a, doped}}$ ) are provided in the last two columns in Table 1. Comparing the activation energy of the doped structure ( $E_{\text{a, doped}}$ ) with that of the Li-stuffed structure in filter 6 ( $E_{\text{a, stuffed}}$ ), it is clear that subvalent doping increases the activation energy by  $0\text{--}80 \text{ meV}$ , slightly decreasing  $\sigma_{\text{rt}}$  by less than one order of magnitude. As a result, all 7 doped compounds still exhibited  $\sigma_{\text{rt, doped}}$  of approximately  $0.1 \text{ mS cm}^{-1}$  or higher except for the Mg-doped  $\text{LiAlO}_2$  ( $\text{Li}_{1+1/32}\text{Mg}_{1/32}\text{Al}_{1-1/32}\text{O}_2$ ) with  $\sigma_{\text{rt, doped}}$  of  $0.02 \text{ mS cm}^{-1}$ . Note that although the compound  $\text{Li}_{3+1/8}\text{Mg}_{1/8}\text{Sc}_{1-1/8}(\text{BO}_3)_2$  in the NASICON regime only exhibits  $\sigma_{\text{rt, doped}}$  of  $0.07 \text{ mS cm}^{-1}$ , a previous computational study showed that its conductivity can reach  $0.1 \text{ mS cm}^{-1}$  when the Li-stuffing degree is tripled.<sup>[44]</sup>

Finally, the 6 Li-stuffed compounds passing the last filter are combined with the pristine compound  $\text{LiGa}(\text{SeO}_3)_2$  into a final list of lithium oxide SIC candidates (Table 2). Their Arrhenius plots and Li-ion probability densities obtained from AIMD simulations are provided in Figures S6–S12, Supporting Information. Based on their Li-ion probability densities, all the candidates indeed have the intended 3D diffusion pathways. For each candidate, information on other compounds in the same structural group is also provided in Tables S4–S9, Supporting Information. It should be noted that  $\text{LiGa}(\text{SeO}_3)_2$  and Mg-doped  $\text{LiSc}(\text{SeO}_3)_2$  actually have the same framework except that Sc cations in  $\text{LiSc}(\text{SeO}_3)_2$  are partially disordered at room temperature, which caused them to be classified into different structural groups in filter 3.

## 3. Discussion

### 3.1. Frameworks of Final Candidates

In a previous study of sulfide-based Li-ion conductors, it was demonstrated that Li-ion migration is likely to be faster in a bcc  $\text{S}^{2-}$  anion framework than in fcc and hcp frameworks.<sup>[40]</sup> Because the high screening power and large size of  $\text{S}^{2-}$  reduce the electrostatic interaction between a Li-ion and the other cations in sulfides, the energy variation along the migration path is, to a large extent, controlled by the changes in anion coordination, a principle that has also been advanced for the migration of other cations.<sup>[81–83]</sup> Diffusion in the bcc framework is expected to be faster because it can occur along a percolating –tet–tet–tet– network that minimizes coordination changes for the migrating Li-ion, whereas in fcc and hcp anion arrangements, jumps between tetrahedral and octahedral sites are required.<sup>[40]</sup> In oxides, the balance of factors that influence the migration energy of Li-ion is different than in sulfides because the lower polarizability of  $\text{O}^{2-}$  anions leads to a more significant interaction between the migrating Li-ion and the other cations. The larger unscreened electrostatic interaction may also facilitate more complex diffusion mechanisms such as cooperative or highly correlated Li hopping.<sup>[42,55,68]</sup> In this paper, using garnet and NASICONs as inspiration, we identify the Li-site

**Table 1.** Summary of properties calculated for filter 6–8 in the high-throughput screening process.  $\sigma_{\text{rt, stuffed}}$  and  $E_{\text{a, stuffed}}$  are the extrapolated room-temperature conductivity and fitted activation energy for the structure with the stuffed Li-ion. Similarly,  $\sigma_{\text{rt, doped}}$  and  $E_{\text{a, doped}}$  are the computed values for the doped structure with the stuffed Li-ion. The error bounds of  $\sigma_{\text{rt, stuffed}}$  and  $\sigma_{\text{rt, doped}}$  were extrapolated considering the error bars of  $E_{\text{a, stuffed}}$  and  $E_{\text{a, doped}}$ .  $E_{\text{defect}}$  and  $E_{\text{above_hull}}$  are the defect formation energy and energy above the hull of the doped structure. Li-stuffing degree = the number of stuffed Li-ions/total number of existing Li-ions in the supercell. Values not passing the corresponding screening criteria are highlighted in bold.

Regime	Pristine comp	ICSD ID	Li-stuffing degree	Filter 6		Filter 7		Filter 8	
				$\sigma_{\text{rt, stuffed}}$ and error bound [mS cm <sup>-1</sup> ]	$E_{\text{a, stuffed}}$ [meV]	$E_{\text{defect}}$ [eV/defect] (doping strategy)	$E_{\text{above_hull}}$ [meV/atom]	$\sigma_{\text{rt, doped}}$ and error bound [mS cm <sup>-1</sup> ]	$E_{\text{a, doped}}$ [meV]
Garnet	Li <sub>4</sub> GeO <sub>4</sub>	18 096	1/64	<b>0.002</b> [10 <sup>-6</sup> , 2.1]	466 ± 172	—*	—	—	—
	Li <sub>4</sub> SiO <sub>4</sub>	238 603	1/112	<b>10<sup>-8</sup></b> [10 <sup>-11</sup> , 10 <sup>-6</sup> ]	920 ± 139	—	—	—	—
	Li <sub>3</sub> PO <sub>4</sub>	257 439	1/48	<b>0.002</b> [10 <sup>-4</sup> , 0.89]	368 ± 100	—	—	—	—
	Li <sub>4</sub> SeO <sub>5</sub>	92 395	1/64	<b>0.04</b> [10 <sup>-5</sup> , 0.24]	395 ± 105	—	—	—	—
	Li <sub>4</sub> SiO <sub>4</sub>	98 615	1/64	1.19 [0.05, 29]	219 ± 79	<b>1.52</b> (Al dopes Si)	10.5	—	—
	Li <sub>2</sub> MgPO <sub>4</sub> F	426 198	1/32	4.84 [0.24, 99]	175 ± 75	<b>1.33</b> (Li dopes Mg)	20.4	—	—
	LiAlO <sub>2</sub>	430 185	1/32	0.27 [0.01, 7.6]	266 ± 83	0.76 (Mg dopes Al)	5.9	<b>0.02</b> [10 <sup>-4</sup> , 2]	333 ± 112
	Li <sub>2</sub> TeO <sub>4</sub>	1485	1/32	6.2 [0.41, 93]	194 ± 67	0.54 (Nb dopes Te)	4.8	2.72 [0.25, 30]	214 ± 59
	Li <sub>6</sub> TeO <sub>6</sub>	26 297	1/48	0.98 [0.07, 14]	248 ± 65	0.58 (Sb dopes Te)	5.5	0.56 [0.05, 6]	262 ± 59
	Li <sub>6</sub> PBrO <sub>5</sub>	421 480	1/24	27 [2.8, 270]	149 ± 57	0.73 (Si dopes P)	13.9	3.2 [0.17, 60]	199 ± 73
NASICON	LiGa(SeO <sub>3</sub> ) <sub>2</sub>	250 868	0	0.21 [0.01, 3.6]	316 ± 70	N/A	0	0.21 [0.01, 3.6]	316 ± 70
	LiSc(SeO <sub>3</sub> ) <sub>2</sub>	239 794	1/4	3.2 [0.08, 122]	216 ± 90	0 (Mg dopes Sc)	0	1 [0.05, 22]	245 ± 77
	Li <sub>4</sub> Ga <sub>3</sub> Si <sub>3</sub> O <sub>12</sub> Cl	87 987	1/8	4.6 [0.14, 145]	198 ± 85	0.79 (Mg dopes Ga)	16.8	0.72 [0.04, 12]	271 ± 70
	Li <sub>3</sub> Sc(BO <sub>3</sub> ) <sub>2</sub>	241 234	1/24	0.18 [0.004, 7.4]	290 ± 92	0.72 (Mg dopes Sc)	7.4	0.07 [0.002, 2.2]	326 ± 88

Filter 6: Long AIMD simulation of stuffed compounds; Filter 7: Dopability; Filter 8: Long AIMD simulation of doped compounds.

topologies that can be activated to harnesses these stronger cation interactions once enough Li is introduced (Li-stuffing).

Indeed, among known lithium oxide SICs, the bcc anion framework has only been observed in Li<sub>3</sub>OCl antiperovskites where there are no non-Li cations, and is not present in other SICs such as garnets, NASICONs, LISICONs, and perovskites. Consistent with this observation, none of our final candidates in Table 2 can be mapped to a bcc anion framework. Instead, the candidate Nb-doped Li<sub>2</sub>TeO<sub>4</sub> ( $\sigma_{\text{rt}} = 2.7 \text{ mS cm}^{-1}$ ) in the garnet regime has a tetragonally distorted inverse spinel structure with an fcc-like anion framework,<sup>[84]</sup> as shown in **Figure 7A,B** for its pristine and doped structures. A Li-based spinel framework has a 3D –tet (8a)–oct (16c)–tet (8a)– Li diffusion network,<sup>[85]</sup> which is topologically equivalent to that of the garnet structure. Furthermore, in both the normal (LiM<sub>2</sub>O<sub>4</sub>) and inverse (Li(LiM)O<sub>4</sub>) spinel, the tetrahedral 8a sites are fully occupied by Li ions while the octahedral 16c sites are vacant, showing the same site occupancy as that in the Li<sub>3</sub> garnet network

(Figure 1B).<sup>[41]</sup> These topological similarities between the spinel and garnet frameworks suggest that they may share the same ion-conduction mechanism. Indeed, the pristine Li<sub>2</sub>TeO<sub>4</sub> has an activation energy of 1.13 eV,<sup>[84]</sup> similar to that in the unstuffed Li<sub>3</sub> garnet.<sup>[8]</sup> Upon Li stuffing, the extra Li-ion (Li<sub>4</sub>) is inserted into the octahedral 16c site and displaces a neighboring tetrahedral 8a Li-ion (Li<sub>2</sub>) to another octahedral 16c site, as illustrated in Figure 7A,B, creating two face-sharing tet–oct Li-ion pairs (Li<sub>1</sub>–Li<sub>4</sub> and Li<sub>2</sub>–Li<sub>3</sub>). Similar face-sharing tet–oct Li-ion configurations have been observed in lithium garnets,<sup>[8,41,52]</sup> in the high-rate spinel Li<sub>4+x</sub>Ti<sub>5</sub>O<sub>12</sub> anode,<sup>[86]</sup> and the partially disordered cation-excess spinel Li<sub>1.68</sub>Mn<sub>1.6</sub>O<sub>3.4</sub>F<sub>0.6</sub>,<sup>[87]</sup> giving rise to high ionic conductivities.<sup>[41,86,88,89]</sup> The same mechanism is likely also present in the Li-stuffed Li<sub>2</sub>TeO<sub>4</sub> accounting for its high predicted conductivity of 2.7 mS cm<sup>-1</sup> (Table 2). Given these similarities between the spinel and garnet frameworks, we believe that the spinel framework is promising for lithium SIC application. Indeed, a lithium halide spinel Li<sub>2</sub>Sc<sub>2/3</sub>Cl<sub>4</sub> was



**Table 2.** Final list of Li superionic oxide conductor candidates from high-throughput screening.  $\sigma_{\text{rt}}$  and  $E_{\text{a}}$  are the extrapolated room-temperature conductivity and activation energy.  $E_{\text{defect}}$  and  $E_{\text{above\_hull}}$  are the defect formation energy and energy above the hull. The error bounds of  $\sigma_{\text{rt}}$  were extrapolated considering the error bars of  $E_{\text{a}}$ .

Regime	Final composition	Source ICSD ID	$\sigma_{\text{rt}}$ and error bound [ $\text{mS cm}^{-1}$ ]	$E_{\text{a}}$ [meV]	$E_{\text{defect}}$ [eV/defect]	$E_{\text{above\_hull}}$ [meV/atom]
Garnet	$\text{Li}_{2+1/16}\text{Nb}_{1/16}\text{Te}_{1-1/16}\text{O}_4$	1485	2.7 [0.25, 30]	$214 \pm 59$	0.54	4.8
	$\text{Li}_{6+1/8}\text{Sb}_{1/8}\text{Te}_{1-1/8}\text{O}_6$	26 297	0.56 [0.05, 6.1]	$262 \pm 59$	0.58	5.5
	$\text{Li}_{6+1/4}\text{Si}_{1/4}\text{P}_{1-1/4}\text{O}_5\text{Br}$	421 480	3.2 [0.17, 60]	$199 \pm 73$	0.73	13.9
NASICON	$\text{LiGa}(\text{SeO}_3)_2$	250 868	0.21 [0.01, 3.6]	$316 \pm 70$	N/A	0
	$\text{Li}_{1+1/4}\text{Mg}_{1/4}\text{Sc}_{1-1/4}(\text{SeO}_3)_2$	239 794	1 [0.05, 22]	$245 \pm 77$	0	0
	$\text{Li}_{4+1/2}\text{Mg}_{1/2}\text{Ga}_{3-1/2}\text{Si}_3\text{O}_{12}\text{Cl}$	87 987	0.72 [0.04, 12]	$271 \pm 70$	0.79	16.8
	$\text{Li}_{3+1/8}\text{Mg}_{1/8}\text{Sc}_{1-1/8}(\text{BO}_3)_2$	241 234	0.07 [0.002, 2.2]	$326 \pm 88$	0.72	7.4

recently reported as a lithium SIC with a high measured ionic conductivity of  $1.5 \text{ mS cm}^{-1}$ .<sup>[90]</sup>

With a value of  $3.2 \text{ mS cm}^{-1}$   $\text{Li}_{6+1/4}\text{Si}_{1/4}\text{P}_{1-1/4}\text{O}_5\text{Br}$  is the candidate compound with the highest predicted ionic conductivity in Table 2. Its pristine structure  $\text{Li}_6\text{PO}_5\text{Br}$  is the oxide version of the sulfide argyrodite  $\text{Li}_6\text{PS}_5\text{X}$  ( $\text{X} = \text{Cl}, \text{Br}, \text{I}$ ) but with a 20% smaller lattice constant.<sup>[91]</sup> Moreover, Li ions in  $\text{Li}_6\text{PO}_5\text{Br}$  reside in the triangular planar center (24g), which differs from the tetrahedral 48h site occupancy in  $\text{Li}_6\text{PS}_5\text{Br}$ .<sup>[22]</sup> These chemical and structural differences make the base compound  $\text{Li}_6\text{PO}_5\text{Br}$  a poor ionic conductor with an activation energy that is 330-meV higher than its sulfide counterpart.<sup>[91]</sup> As shown in Figure 7C, extra Li in  $\text{Li}_6\text{PO}_5\text{Br}$  is accommodated in the interstitial tetrahedral 16e site (Li3) where it face-shares with two 24g Li-ions (Li1 and Li2), likely facilitating the rate-limiting inter-cage diffusion.<sup>[92]</sup> The same occupancy of excess Li has been recently observed in the Li-stuffed argyrodites  $\text{Li}_{4.1}\text{Al}_{0.1}\text{Si}_{0.9}\text{S}_4$ <sup>[24]</sup> and  $\text{Li}_{6.15}\text{Al}_{0.15}\text{Si}_{1.35}\text{S}_{5.4}\text{O}_{0.6}$ .<sup>[93]</sup> Therefore, our result demonstrates that the oxy-argyrodite framework can allow fast Li-ion conduction once an excess amount of Li is stuffed into the structure, similar to its sulfide counterpart.<sup>[94]</sup>

The candidate  $\text{Li}_{4+1/2}\text{Mg}_{1/2}\text{Ga}_{3-1/2}\text{Si}_3\text{O}_{12}\text{Cl}$  ( $\sigma_{\text{rt}} = 0.72 \text{ mS cm}^{-1}$ ) is Mg-doped  $\text{Li}_4\text{Ga}_3\text{Si}_3\text{O}_{12}\text{Cl}$  which has the sodalite structure.<sup>[95,96]</sup> Similar to the argyrodite framework, the sodalite framework also features space-filling cages.<sup>[97]</sup> Each sodalite cage has a  $\text{Cl}^-$  ion in its center tetrahedrally coordinated by 4 Li-ions, forming a  $\text{Li}_4\text{Cl}$  cluster.<sup>[96]</sup> The pristine compound has an activation energy for Li migration ranging from 0.83 to 0.95 eV.<sup>[98]</sup> Li stuffing is achieved with Li (Li9) in an unoccupied tetrahedral site in a sodalite cage, forming a local  $\text{Li}_5\text{Cl}$  cluster and face-sharing with another tetrahedral Li-ion (Li5) in a neighboring cage, as illustrated in Figure 7D. The face-sharing tet-tet Li-ion configuration is likely the key factor promoting inter-cage diffusion, as for the  $\text{Li}_{6+1/4}\text{Si}_{1/4}\text{P}_{1-1/4}\text{O}_5\text{Br}$  argyrodite, which drastically reduces the activation energy to only 271 meV (Table 2). We note that the sodalite framework is a robust framework that can accommodate a wide range of cation and anion combinations. For example, 10 compositions for Li oxide

sodalites extracted from ICSD are listed in Table S8, Supporting Information. The large chemical space for sodalite compounds creates new possibilities to further optimize its ionic conductivity and dopability, making this framework attractive for further exploration.

$\text{LiM}(\text{SeO}_3)_2$  ( $\text{M} = \text{Ga},^{[99]} \text{Sc},^{[100]} \text{Fe}^{[101]}$ ) in the NASICON regime presents an intriguing new framework where both the pristine composition  $\text{LiGa}(\text{SeO}_3)_2$  and the Li-stuffed composition  $\text{Li}_{1+1/4}\text{Mg}_{1/4}\text{Sc}_{1-1/4}(\text{SeO}_3)_2$  are predicted to have ionic conductivity above  $0.1 \text{ mS cm}^{-1}$  (Table 2). The crystal structure of  $\text{LiGa}(\text{SeO}_3)_2$  and Li-ion probability density from AIMD simulation are shown in Figure 7E,F. There are several interesting features of the framework that can be compared with those in the NASICON framework. First, Li ions in the pristine  $\text{LiM}(\text{SeO}_3)_2$  reside in highly distorted tetrahedral sites<sup>[99,101]</sup> (Figure 7E), similar to the distorted 6b Li sites in the pristine NASICON. The distortion of Li sites has been considered beneficial for frustrating the energy landscape for Li-ion conduction.<sup>[102]</sup> Second, it has the intended homogeneity of the transport path, as indicated by the equivalent gap sizes in all three dimensions (Table S7, Supporting Information). Third, the  $\text{LiM}(\text{SeO}_3)_2$  framework has intermediate low-energy vacant sites (“site X” in Figure 7F with high Li-ion probability density) between occupied Li sites, which is similar to the unoccupied M2 (18e) sites between occupied M1 (6b) sites in the NASICON framework.<sup>[55,103]</sup> These low-energy vacant sites can bridge the large gap between neighboring Li-ions and facilitate Li-ion conduction. These similarities between the  $\text{LiM}(\text{SeO}_3)_2$  and NASICON frameworks make  $\text{LiM}(\text{SeO}_3)_2$  an intriguing candidate for SIC application. Furthermore, DFT results show that upon Li stuffing, the stuffed Li-ion is inserted into the low-energy site X (Figure S10A, Supporting Information), explaining the excellent dopability ( $E_{\text{defect}} = 0 \text{ eV/defect}$ ) of the  $\text{LiM}(\text{SeO}_3)_2$  framework.

### 3.2. Effect of Li-Stuffing Amount

In the current work, we did not study in detail the effect of Li concentration once the diffusion network is activated. In our

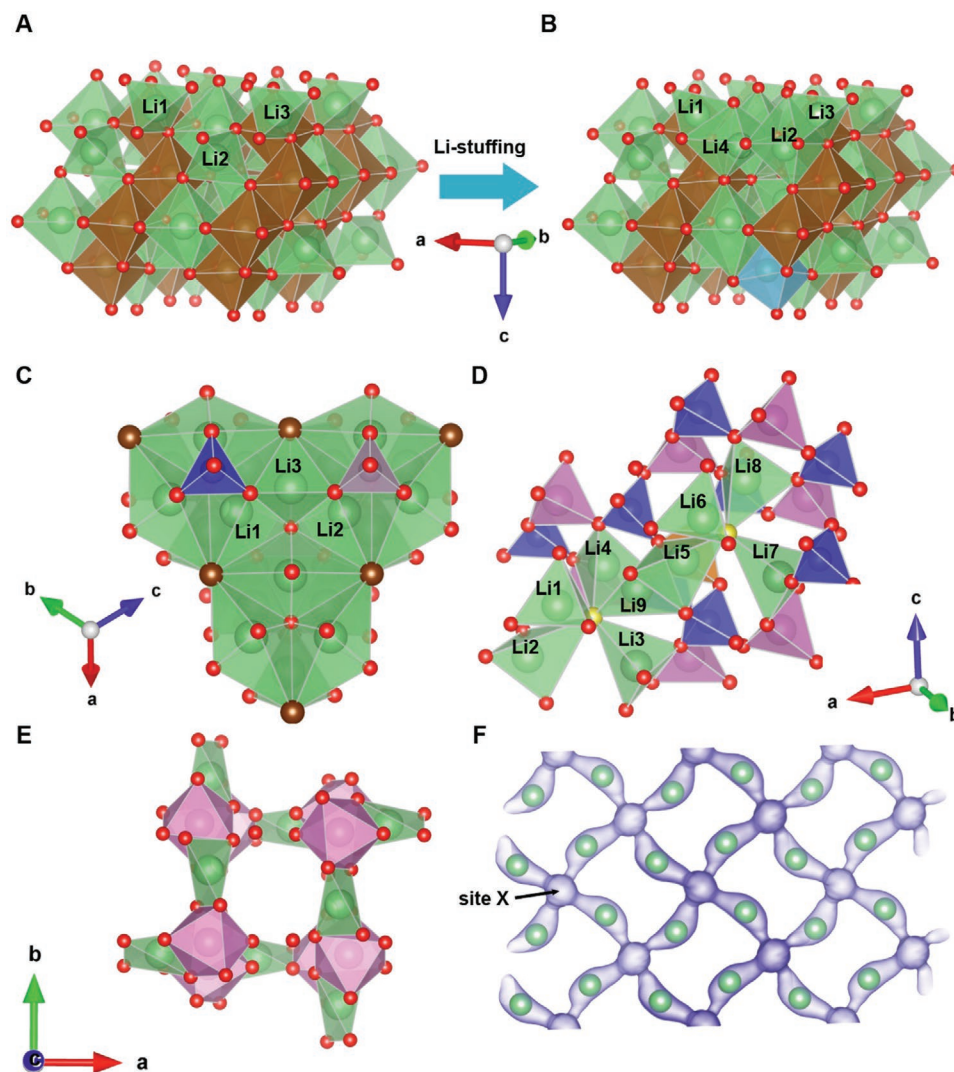


**Figure 7.** Examples of lithium oxide SIC candidates. A,B) Crystal structure of  $\text{Li}_2\text{TeO}_4$  before (A) and after (B) Li stuffing via Nb doping. Li1–3: Li ions in the pristine compound. Li4: the stuffed Li-ion. C) Crystal structure of  $\text{Li}_{6+1/4}\text{Si}_{1/4}\text{P}_{1-1/4}\text{O}_5\text{Br}$ . Li1–2: Li ions in the pristine compound. Li3: the stuffed Li-ion. D) Crystal structure of  $\text{Li}_{4+1/2}\text{Mg}_{1/2}\text{Ga}_{3-1/2}\text{Si}_3\text{O}_{12}\text{Cl}$ . Li1–8: Li-ions in the pristine compound. Li9: the stuffed Li-ion. E,F) Crystal structure of  $\text{LiGa}(\text{SeO}_3)_2$  (E) and the isosurface of Li-ion probability density from AIMD simulation at 1000 K (F). Isovalue  $P = P_{\text{max}} / 50$ , where  $P_{\text{max}}$  is the maximum value of the density. Site X is the intermediate vacant site between neighboring occupied Li sites. Green polyhedrons:  $\text{LiO}_x$ , brown octahedrons:  $\text{TeO}_6$ , light blue polyhedrons:  $\text{NbO}_6$ , dark blue tetrahedrons:  $\text{SiO}_4$ , orange octahedrons:  $\text{MgO}_4$ , purple polyhedrons:  $\text{PO}_4$ , pink polyhedrons:  $\text{GaO}_x$ .  $\text{SeO}_3$  groups are omitted for clarity. Green spheres: Li-ions, yellow spheres:  $\text{Cl}^-$  anions, brown spheres:  $\text{Br}^-$  anions, red spheres:  $\text{O}^{2-}$  anions.

“activated diffusion network” model, a single stuffed Li-ion should in principle be sufficient to activate one quiescent local environment and create a steep increase in ionic conductivity. Therefore, for simplicity, we only stuffed one Li-ion into a supercell during the high-throughput screening. As a result, the Li-stuffing degree was generally low in these materials, in particular for those in the garnet regime where the Li-stuffing degree is typically below 5% (Table 1). This still leaves considerable room to increase the ionic conductivity by modifying the Li content. For example, in the candidate compound  $\text{Li}_{3+x}\text{Mg}_x\text{Sc}_{1-x}(\text{BO}_3)_2$  increasing  $x$  from  $1/8$  to  $3/8$  increases the ionic conductivity from 0.07 to 0.1  $\text{mS cm}^{-1}$ .<sup>[44]</sup> However, the metastability of the compound measured by  $E_{\text{above hull}}$  is also increased from 7.4 to 21 meV/atom.<sup>[44]</sup> This is because as the Li-stuffing degree increases, the number of activated local

environments increases, providing more carriers for ionic conduction but also making the structure less stable. Therefore, the often observed trade-off between ionic conductivity and stability in SIC development<sup>[4]</sup> should be considered when tuning the Li-stuffing degree. In this context, it should be pointed out that the Li-excess and the extra entropy they create may somewhat help stabilize these compounds at their synthesis temperatures.<sup>[26,104]</sup>

As the Li-stuffing degree increases beyond the dilute limit, its effect becomes more difficult to predict. For example, as the Li concentration in garnet increases toward Li7, the dominant Li-ion triplet arrangement changes from the tet–oct–tet type to the oct–tet–oct type, leading to a different ion-conduction mechanism than that in the  $\text{Li}_{3+\delta}$  garnet.<sup>[41,52,88]</sup> Eventually, the ionic conductivity is expected to decrease with the Li-stuffing

degree once the low vacancy concentration becomes a limiting factor for Li-ion conduction.

### 3.3. Limitations and New Possibilities

Earlier work using Li diffusion network analysis focused on determining the potential sites for the mobile ion, migration channel size, and dimensionality of the conduction network.<sup>[105–108]</sup> Recent work by He et al. also considered the presence of “enlarged Li sites” in the network as a key feature for lithium SICs and used it as a screening criterion to find new SICs.<sup>[44]</sup> In the present work, we demonstrated two new site-network features specific for oxide SICs. By laying out how occupied and intermediate Li sites should be connected to harness the coulombic repulsion that arises when extra Li is added, we have been able to identify several new potential fast Li-ion conductors. We proposed a small max gap size along the path between occupied Li sites and the homogeneity of the transport path as key elements for oxide Li-ion conductors. The small max gap size ensures that when extra Li is inserted the strong coulombic interaction between the excess Li and the framework Li creates a mobile defect. The homogeneity of the transport path ensures that these mobile defects do not get trapped. The fact that we rediscover known frameworks such as argyrodites or spinels and novel frameworks such as  $\text{LiM}(\text{SeO}_3)_2$  successfully validates that our hypothesized structural and topological features for garnet-like and NASICON-like diffusion are not unique to them, but are applicable to other materials. Successes in predicting new lithium SICs based on these network features highlight the usefulness of geometrical–topological analysis in the study of SICs.

The objective of our search was to identify some new frameworks that offer the potential for good Li-ion conductivity, but it needs to be stressed that simplifications in our analysis may have led us to overlook compounds as possible fast Li-ion conductors. First, the representative transport path is assumed to be the one with the smallest max gap size, and the stuffed Li-ion is assumed to be inserted into this path. In reality, the failure of either assumption will make the min-max gap size analysis (filter 2) less relevant. Second, results from the 10-ps short AIMD simulation (filter 5) suffer from high statistical variance, which may lead to false negatives in the screening process that cannot be detected downstream. Third, we only selected one composition from each structural group in filter 3 and only selected one doped structure for AIMD simulation in filter 8, it is possible that the selected chemistries were not optimal for ionic conductivity or dopability. Some of these limitations can be addressed by more fully exploring the chemical space of promising frameworks including the spinel, oxy-argyrodite, sodalite, and  $\text{LiM}(\text{SeO}_3)_2$  frameworks.

Our approach for finding new lithium oxide SICs is in principle applicable to other ionic conductors (e.g.,  $\text{Na}^+$  and  $\text{Ca}^{2+}$  mobile ions) and other anion chemistries (e.g., sulfides, nitrides, and chlorides). However, the strength of coulombic interactions between mobile ions in those systems may vary depending on the specific cation and anion chemistries. For example, the coulombic force between two  $\text{Ca}^{2+}$  ions will be four times stronger than that for Li-ions at the same separation

which may enhance the tendency for collective motion but also the instability when excess divalent ion is added to the structure. In contrast, because of their larger size and larger polarizability of  $\text{S}^{2-}$  anions,<sup>[40]</sup> the coulombic interaction between Li-ions in sulfides is weaker than that in oxides. We hypothesize that this makes Li-stuffing less effective.

## 4. Conclusion

In summary, by exploring the Li-ion conduction mechanisms in Li-stuffed garnet and NASICON, a common pattern of an “activated diffusion network” was identified. Three network features were hypothesized to be beneficial for enabling this pattern: a 3D percolation Li diffusion network, a small gap size between occupied Li sites, and the homogeneity of the transport path. A high-throughput screening for compounds that share these features and could be Li stuffed revealed several new structure classes as potential fast Li-ion conductors, validating our proposed features. Using more elaborate first-principles calculations to evaluate the room-temperature ionic conductivity and dopability of the candidate structures, we proposed 7 compounds as promising lithium oxide SIC candidates. Moreover, several intriguing frameworks emerged for the future development of lithium oxide SICs, including the spinel, oxy-argyrodite, sodalite, and  $\text{LiM}(\text{SeO}_3)_2$  frameworks.

## 5. Experimental Section

**Structure Grouping:** Structure grouping was performed using the Structure Matcher in the pymatgen software package.<sup>[75]</sup> The structure from the ICSD was preprocessed sequentially by 1) replacing the disordered sites with the species having the highest site occupancy, 2) replacing non-Li cations with a dummy cation, 3) replacing all anions with  $\text{O}^{2-}$ , and 4) removing all Li sites. Two structures were in the same group if their unit cells or primitive cells could be matched with distortions smaller than the default thresholds.

**First-Principles Calculations:** All the DFT calculations were performed within the projector augmented wave (PAW) formalism<sup>[109]</sup> as implemented in the Vienna ab initio simulation package (VASP).<sup>[110]</sup> For the exchange-correlational functional, a mixed scheme of the generalized gradient approximation (GGA)<sup>[111]</sup> and GGA with the rotationally invariant Hubbard (+U) correction<sup>[112,113]</sup> was employed, as described in the work by Jain et al.<sup>[114]</sup>

**NEB Method:** NEB calculations<sup>[115]</sup> were performed in DFT for the Li-stuffed garnet  $\text{Li}_{3+1/8}\text{La}_3\text{Te}_2\text{O}_{12}$  with the initial and final Li-ion configurations shown in Figure 2B and Figure 2C, respectively. The charge of the stuffed Li-ion was compensated by a uniform background charge to retain the oxidation state for all ions. An energy cut-off of 400 eV, a gamma-point-only sampling of k-space, and 5 intermediate images were used. The NEB calculation was performed at constant volume and was non-spin-polarized.

**AIMD Simulations:** AIMD simulations were performed in VASP at temperatures between 800 and 1300 K. A timestep of 2 fs was selected. At the beginning of the simulation, the temperature was set at 100 K according to a Boltzmann distribution. Next, the temperature was ramped up to the target temperature in 2 ps by velocity scaling, after which the supercell was equilibrated at the target temperature for 5 ps in the NVT ensemble with a Nosé–Hoover thermostat.<sup>[116,117]</sup> After equilibrium, AIMD simulations were continued in the NVT ensemble at the target temperature for another 10 ps for short AIMD simulations (filter 5) or at least 100 ps for long AIMD simulations (filter 6 and filter 8). An energy cut-off of 400 eV and a gamma-point-only sampling of k-space



were used. All the calculations were performed at constant volume and were non-spin-polarized. The analyses of AIMD results used the scheme proposed by He et al.<sup>[118]</sup> The Li-ion conductivity was computed from diffusion coefficient using the Nernst–Einstein approximation. The Li-ion probability density calculation was performed using the scheme proposed by Wang et al.<sup>[40]</sup> For all the analyses above, the data point was excluded if melting was observed.

**Site for the Stuffed Li-ion:** For a given crystal structure, the candidate sites for Li stuffing were the 20 symmetrically distinct vacant Li sites with the lowest energies modeled by the Buckingham potential.<sup>[119]</sup> DFT calculations were performed on the 20 supercells, each with a stuffed Li-ion in a candidate site and with a uniform background charge. The candidate site associated with the lowest DFT energy was selected as the site for the stuffed Li-ion. An energy cut-off of 400 eV and a k-point grid of at least 1000/(number of atoms) were used. All the calculations were performed at constant volume and were non-spin-polarized.

**Dopability:** The defect formation energy ( $E_{\text{defect}}$ ) was calculated as

$$E_{\text{defect}} = E_{\text{doped}} - E_{\text{pristine}} + \sum_i \Delta n_i \mu_i \quad (2)$$

Here,  $E_{\text{doped}}$  and  $E_{\text{pristine}}$  are the bulk energies of the doped and pristine structures, respectively.  $\Delta n_i$  is the number of atoms of element  $i$  being added to or removed from the supercell during the doping, and  $\mu_i$  is the chemical potential of element  $i$  at the pristine composition. For the bulk energy calculations of pristine and doped compounds, an energy cut-off of 520 eV and a k-point grid of at least 1000/(number of atoms) were used.

To calculate the energy above the hull ( $E_{\text{above_hull}}$ ) of the doped structure, the lower energy convex hull was constructed using all ground-state phases (including the doped structure) in the chemical space defined by elements in the doped composition using the pymatgen software package.<sup>[75]</sup>  $E_{\text{above_hull}}$  was defined as the energy of the doped structure above the lower convex hull. An  $E_{\text{above_hull}}$  value of 0 eV/atom means that the doped structure was precisely on the hull and therefore thermodynamically stable.

## Supporting Information

Supporting Information is available from the Wiley Online Library or from the author.

## Acknowledgements

Y.X. and K.J. contributed equally to this work. This work was supported by the Samsung Advanced Institute of Technology and the Assistant Secretary of Energy Efficiency and Renewable Energy, Vehicle Technologies Office of the US Department of Energy (DOE) under contract no. DE-AC02-05CH11231 under the Advanced Battery Materials Research (BMR) Program. This research used resources of the National Energy Research Scientific Computing Center (NERSC), a U.S. Department of Energy Office of Science User Facility operated under Contract No. DE-AC02-05CH11231, and the Extreme Science and Engineering Discovery Environment (XSEDE), which is supported by the National Science Foundation grant number ACI-1548562.

## Conflict of Interest

The authors declare no conflict of interest.

## Data Availability Statement

The data that support the findings of this study are available from the corresponding author upon reasonable request.

## Keywords

batteries, DFT calculations, solid electrolytes, solid-state batteries, superionic conductors

Received: May 7, 2021

Revised: July 14, 2021

Published online:

- [1] J. Janek, W. G. Zeier, *Nat. Energy* **2016**, *1*, 16141.
- [2] J. C. Bachman, S. Muy, A. Grimaud, H.-H. Chang, N. Pour, S. F. Lux, O. Paschos, F. Maglia, S. Lupat, P. Lamp, L. Giordano, Y. Shao-Horn, *Chem. Rev.* **2016**, *116*, 140.
- [3] W. D. Richards, L. J. Miara, Y. Wang, J. C. Kim, G. Ceder, *Chem. Mater.* **2016**, *28*, 266.
- [4] Y. Xiao, Y. Wang, S.-H. Bo, J. C. Kim, L. J. Miara, G. Ceder, *Nat. Rev. Mater.* **2020**, *5*, 105.
- [5] Y. Zhu, X. He, Y. Mo, *ACS Appl. Mater. Interfaces* **2015**, *7*, 23685.
- [6] Y. Zhu, X. He, Y. Mo, *J. Mater. Chem. A* **2016**, *4*, 3253.
- [7] A. Manthiram, X. Yu, S. Wang, *Nat. Rev. Mater.* **2017**, *2*, 16103.
- [8] V. Thangadurai, S. Narayanan, D. Pinzaru, *Chem. Soc. Rev.* **2014**, *43*, 4714.
- [9] N. Anantharamulu, K. K. Rao, G. Rambabu, B. V. Kumar, V. Radha, M. Vithal, *J. Mater. Sci.* **2011**, *46*, 2821.
- [10] X. Yu, J. B. Bates, G. E. Jellison, F. X. Hart, *J. Electrochem. Soc.* **1997**, *144*, 524.
- [11] Y. Zhao, L. L. Daemen, *J. Am. Chem. Soc.* **2012**, *134*, 15042.
- [12] S. Stramare, V. Thangadurai, W. Weppner, *Chem. Mater.* **2003**, *15*, 3974.
- [13] H. Y.-P. Hong, *Mater. Res. Bull.* **1978**, *13*, 117.
- [14] P. G. Bruce, A. R. West, *J. Solid State Chem.* **1982**, *44*, 354.
- [15] S. Li, J. Zhu, Y. Wang, J. W. Howard, X. Lü, Y. Li, R. S. Kumar, L. Wang, L. L. Daemen, Y. Zhao, *Solid State Ionics* **2016**, *284*, 14.
- [16] J. A. Dawson, T. S. Attari, H. Chen, S. P. Emge, K. E. Johnston, M. S. Islam, *Energy Environ. Sci.* **2018**, *11*, 2993.
- [17] A. Hayashi, S. Hama, H. Morimoto, M. Tatsumisago, T. Minami, *J. Am. Ceram. Soc.* **2001**, *84*, 477.
- [18] Y. Seino, T. Ota, K. Takada, A. Hayashi, M. Tatsumisago, *Energy Environ. Sci.* **2014**, *7*, 627.
- [19] N. Kamaya, K. Homma, Y. Yamakawa, M. Hirayama, R. Kanno, M. Yonemura, T. Kamiyama, Y. Kato, S. Hama, K. Kawamoto, A. Mitsui, *Nat. Mater.* **2011**, *10*, 682.
- [20] Y. Kato, S. Hori, T. Saito, K. Suzuki, M. Hirayama, A. Mitsui, M. Yonemura, H. Iba, R. Kanno, *Nat. Energy* **2016**, *1*, 16030.
- [21] S. P. Ong, Y. Mo, W. D. Richards, L. Miara, H. S. Lee, G. Ceder, *Energy Environ. Sci.* **2013**, *6*, 148.
- [22] H.-J. Deiseroth, S.-T. Kong, H. Eckert, J. Vannahme, C. Reiner, T. Zaiß, M. Schloßer, *Angew. Chem., Int. Ed.* **2008**, *47*, 755.
- [23] R. P. Rao, S. Adams, *Phys. Status Solidi A* **2011**, *208*, 1804.
- [24] W. Huang, K. Yoshino, S. Hori, K. Suzuki, M. Yonemura, M. Hirayama, R. Kanno, *J. Solid State Chem.* **2019**, *270*, 487.
- [25] Z. Liu, W. Fu, E. A. Payzant, X. Yu, Z. Wu, N. J. Dudney, J. Kiggans, K. Hong, A. J. Rondinone, C. Liang, *J. Am. Chem. Soc.* **2013**, *135*, 975.
- [26] L. Zhou, A. Assoud, A. Shyamsunder, A. Huq, Q. Zhang, P. Hartmann, J. Kulisch, L. F. Nazar, *Chem. Mater.* **2019**, *31*, 7801.
- [27] W. D. Richards, Y. Wang, L. J. Miara, J. C. Kim, G. Ceder, *Energy Environ. Sci.* **2016**, *9*, 3272.
- [28] N. Suzuki, W. D. Richards, Y. Wang, L. J. Miara, J. C. Kim, I.-S. Jung, T. Tsujimura, G. Ceder, *Chem. Mater.* **2018**, *30*, 2236.
- [29] K. Kaup, F. Lalère, A. Huq, A. Shyamsunder, T. Adermann, P. Hartmann, L. F. Nazar, *Chem. Mater.* **2018**, *30*, 592.
- [30] Q. Zhao, S. Stalin, C.-Z. Zhao, L. A. Archer, *Nat. Rev. Mater.* **2020**, *5*, 229.

- [31] C. Wang, K. Fu, S. P. Kammampata, D. W. McOwen, A. J. Samson, L. Zhang, G. T. Hitz, A. M. Nolan, E. D. Wachsman, Y. Mo, V. Thangadurai, L. Hu, *Chem. Rev.* **2020**, 120, 4257.
- [32] Y.-F. Y. Yao, J. T. Kummer, *J. Inorg. Nucl. Chem.* **1967**, 29, 2453.
- [33] J. B. Goodenough, H. Y.-P. Hong, J. A. Kafalas, *Mater. Res. Bull.* **1976**, 11, 203.
- [34] H. Y.-P. Hong, *Mater. Res. Bull.* **1976**, 11, 173.
- [35] Y. Inaguma, C. Liqun, M. Itoh, T. Nakamura, T. Uchida, H. Ikuta, M. Wakihara, *Solid State Commun.* **1993**, 86, 689.
- [36] V. Thangadurai, H. Kaack, W. J. F. Weppner, *J. Am. Ceram. Soc.* **2003**, 86, 437.
- [37] R. Murugan, V. Thangadurai, W. Weppner, *Angew. Chem., Int. Ed.* **2007**, 46, 7778.
- [38] G. Schwering, A. Hönnerscheid, L. van Wüllen, M. Jansen, *ChemPhysChem* **2003**, 4, 343.
- [39] K. Takada, *Acta Mater.* **2013**, 61, 759.
- [40] Y. Wang, W. D. Richards, S. P. Ong, L. J. Miara, J. C. Kim, Y. Mo, G. Ceder, *Nat. Mater.* **2015**, 14, 1026.
- [41] R. Jalem, Y. Yamamoto, H. Shiiba, M. Nakayama, H. Munakata, T. Kasuga, K. Kanamura, *Chem. Mater.* **2013**, 25, 425.
- [42] X. He, Y. Zhu, Y. Mo, *Nat. Commun.* **2017**, 8, 15893.
- [43] B. Kozinsky, S. A. Akhade, P. Hirel, A. Hashibon, C. Elsässer, P. Mehta, A. Logeat, U. Eisele, *Phys. Rev. Lett.* **2016**, 116, 055901.
- [44] X. He, Q. Bai, Y. Liu, A. M. Nolan, C. Ling, Y. Mo, *Adv. Energy Mater.* **2019**, 9, 1902078.
- [45] L. Kahle, A. Marcolongo, N. Marzari, *Energy Environ. Sci.* **2020**, 13, 928.
- [46] X. Feng, P.-H. Chien, S. Patel, Y. Wang, Y.-Y. Hu, *Chem. Mater.* **2020**, 32, 3036.
- [47] S. Xiong, X. He, A. Han, Z. Liu, Z. Ren, B. McElhenny, A. M. Nolan, S. Chen, Y. Mo, H. Chen, *Adv. Energy Mater.* **2019**, 9, 1803821.
- [48] Q. Wang, J.-F. Wu, Z. Lu, F. Ciucci, W. K. Pang, X. Guo, *Adv. Funct. Mater.* **2019**, 29, 1904232.
- [49] A. Belsky, M. Hellenbrandt, V. L. Karen, P. Luksch, *Acta Crystallogr. B* **2002**, 58, 364.
- [50] H. Xie, J. A. Alonso, Y. Li, M. T. Fernández-Díaz, J. B. Goodenough, *Chem. Mater.* **2011**, 23, 3587.
- [51] C. A. Geiger, E. Alekseev, B. Lazic, M. Fisch, T. Armbruster, R. Langner, M. Fechtelkord, N. Kim, T. Pettke, W. Weppner, *Inorg. Chem.* **2011**, 50, 1089.
- [52] M. Xu, M. S. Park, J. M. Lee, T. Y. Kim, Y. S. Park, E. Ma, *Phys. Rev. B* **2012**, 85, 052301.
- [53] Y. Chen, E. Rangasamy, C. Liang, K. An, *Chem. Mater.* **2015**, 27, 5491.
- [54] M. P. O'Callaghan, E. J. Cussen, *Chem. Commun.* **2007**, 2048.
- [55] B. Lang, B. Ziebarth, C. Elsässer, *Chem. Mater.* **2015**, 27, 5040.
- [56] M. Aykol, S. Kim, V. I. Hegde, S. Kirklin, C. Wolverton, *Phys. Rev. Mater.* **2019**, 3, 025402.
- [57] M. P. O'Callaghan, A. S. Powell, J. J. Titman, G. Z. Chen, E. J. Cussen, *Chem. Mater.* **2008**, 20, 2360.
- [58] M. Kotobuki, K. Kanamura, *Ceram. Int.* **2013**, 39, 6481.
- [59] Y. Li, J. -T. Han, C. -A. Wang, H. Xie, J. B. Goodenough, *J. Mater. Chem.* **2012**, 22, 15357.
- [60] Y. Wang, W. Lai, *Electrochem. Solid-State Lett.* **2012**, 15, A68.
- [61] S. Hamdoun, D. T. Qui, E. J. L. Schouler, *Solid State Ionics* **1986**, 18–19, 587.
- [62] H. Aono, E. Sugimoto, Y. Sadaoka, N. Imanaka, G. Adachi, *J. Electrochem. Soc.* **1990**, 137, 1023.
- [63] K. Arbi, S. Mandal, J. M. Rojo, J. Sanz, *Chem. Mater.* **2002**, 14, 1091.
- [64] N. V. Kosova, E. T. Devyatkina, A. P. Stepanov, A. L. Buzlukov, *Ionics* **2008**, 14, 303.
- [65] K. Arbi, J. M. Rojo, J. Sanz, *J. Eur. Ceram. Soc.* **2007**, 27, 4215.
- [66] X. Lu, S. Wang, R. Xiao, S. Shi, H. Li, L. Chen, *Nano Energy* **2017**, 41, 626.
- [67] K. Arbi, M. Hoelzel, A. Kuhn, F. García-Alvarado, J. Sanz, *Inorg. Chem.* **2013**, 52, 9290.
- [68] Y. A. Du, N. A. W. Holzwarth, *J. Electrochem. Soc.* **2007**, 154, A999.
- [69] F. H. Stillinger, *Science* **1995**, 267, 1935.
- [70] S. Sastry, P. G. Debenedetti, F. H. Stillinger, *Nature* **1998**, 393, 554.
- [71] P. G. Debenedetti, F. H. Stillinger, *Nature* **2001**, 410, 259.
- [72] R. Malik, D. Burch, M. Bazant, G. Ceder, *Nano Lett.* **2010**, 10, 4123.
- [73] J. O'Rourke, *Computational Geometry in C*, Cambridge University Press, Cambridge **1998**.
- [74] M. D. Foster, I. Rivin, M. M. J. Treacy, O. Delgado Friedrichs, *Microporous Mesoporous Mater.* **2006**, 90, 32.
- [75] S. P. Ong, W. D. Richards, A. Jain, G. Hautier, M. Kocher, S. Cholia, D. Gunter, V. L. Chevrier, K. A. Persson, G. Ceder, *Comput. Mater. Sci.* **2013**, 68, 314.
- [76] Y. Meesala, A. Jena, H. Chang, R.-S. Liu, *ACS Energy Lett.* **2017**, 2, 2734.
- [77] A. Jain, S. P. Ong, G. Hautier, W. Chen, W. D. Richards, S. Dacek, S. Cholia, D. Gunter, D. Skinner, G. Ceder, K. A. Persson, *APL Mater.* **2013**, 1, 011002.
- [78] L. J. Miara, W. D. Richards, Y. E. Wang, G. Ceder, *Chem. Mater.* **2015**, 27, 4040.
- [79] S.-H. Bo, Y. Wang, J. C. Kim, W. D. Richards, G. Ceder, *Chem. Mater.* **2016**, 28, 252.
- [80] G. Hautier, C. Fischer, V. Ehrlacher, A. Jain, G. Ceder, *Inorg. Chem.* **2011**, 50, 656.
- [81] Z. Rong, R. Malik, P. Canepa, G. S. Gautam, M. Liu, A. Jain, K. Persson, G. Ceder, *Chem. Mater.* **2015**, 27, 6016.
- [82] G. S. Gautam, P. Canepa, A. Abdellahi, A. Urban, R. Malik, G. Ceder, *Chem. Mater.* **2015**, 27, 3733.
- [83] G. S. Gautam, P. Canepa, R. Malik, M. Liu, K. Persson, G. Ceder, *Chem. Commun.* **2015**, 51, 13619.
- [84] C. González, M. L. López, M. Gaitán, M. L. Veiga, C. Pico, *Mater. Res. Bull.* **1994**, 29, 903.
- [85] D. Z. C. Martin, A. R. Haworth, W. L. Schmidt, P. J. Baker, R. Boston, K. E. Johnston, N. Reeves-McLaren, *Phys. Chem. Chem. Phys.* **2019**, 21, 23111.
- [86] W. Zhang, D.-H. Seo, T. Chen, L. Wu, M. Topsakal, Y. Zhu, D. Lu, G. Ceder, F. Wang, *Science* **2020**, 367, 1030.
- [87] H. Ji, J. Wu, Z. Cai, J. Liu, D.-H. Kwon, H. Kim, A. Urban, J. K. Papp, E. Foley, Y. Tian, M. Balasubramanian, H. Kim, R. J. Clément, B. D. McCloskey, W. Yang, G. Ceder, *Nat. Energy* **2020**, 5, 213.
- [88] Y. Wang, A. Huq, W. Lai, *Solid State Ionics* **2014**, 255, 39.
- [89] S. Ganapathy, A. Vasileiadis, J. R. Heringa, M. Wagemaker, *Adv. Energy Mater.* **2017**, 7, 1601781.
- [90] L. Zhou, C. Y. Kwok, A. Shyamsunder, Q. Zhang, X. Wu, L. Nazar, *Energy Environ. Sci.* **2020**, 13, 2056.
- [91] S.-T. Kong, H.-J. Deiseroth, J. Maier, V. Nickel, K. Weichert, C. Reiner, *Z. Anorg. Chem.* **2010**, 636, 1920.
- [92] N. J. J. de Klerk, I. Rosłóń, M. Wagemaker, *Chem. Mater.* **2016**, 28, 7955.
- [93] W. Huang, C. LinDong, S. Hori, K. Suzuki, M. Yonemura, M. Hirayama, R. Kanno, *Mater. Adv.* **2020**, 1, 334.
- [94] L. Zhou, N. Minafra, W. G. Zeier, L. F. Nazar, *Acc. Chem. Res.* **2021**, 54, 2717.
- [95] L. Pauling, *Z. Kristallogr. Cryst. Mater.* **1930**, 74, 213.
- [96] G. M. Johnson, M. T. Weller, *Inorg. Chem.* **1999**, 38, 2442.
- [97] I. Hassan, H. D. Grundy, *Acta Crystallogr. B* **1984**, 40, 6.
- [98] G. Kelemen, W. Lortz, G. Schön, *J. Mater. Sci.* **1989**, 24, 333.
- [99] D. W. Lee, K. M. Ok, *Inorg. Chem.* **2013**, 52, 5176.
- [100] S. Y. Song, K. M. Ok, *Cryst. Growth Des.* **2016**, 16, 3076.
- [101] G. Giester, *Monatsh. Für Chem. Chem. Mon.* **1994**, 125, 535.
- [102] D. D. Stefano, A. Miglio, K. Robeyns, Y. Filinchuk, M. Lechartier, A. Senyshyn, H. Ishida, S. Spannenberger, D. Prutsch, S. Lunghammer, D. Rettenwander, M. Wilkening, B. Roling, Y. Kato, G. Hautier, *Chem* **2019**, 5, 2450.

- [103] A. Aatiq, M. Ménétrier, L. Croguennec, E. Suard, C. Delmas, *J. Mater. Chem.* **2002**, 12, 2971.
- [104] V. S. Kandagal, M. D. Bharadwaj, U. V. Waghmare, *J. Mater. Chem. A* **2015**, 3, 12992.
- [105] V. A. Blatov, G. D. Ilyushin, O. A. Blatova, N. A. Anurova, A. K. Ivanov-Schits, L. N. Dem'yanets, *Acta Crystallogr. B* **2006**, 62, 1010.
- [106] N. A. Anurova, V. A. Blatov, G. D. Ilyushin, O. A. Blatova, A. K. Ivanov-Schitz, L. N. Dem'yanets, *Solid State Ionics* **2008**, 179, 2248.
- [107] N. A. Anurova, V. A. Blatov, *Acta Crystallogr. B* **2009**, 65, 426.
- [108] F. Meutzner, W. Münchgesang, N. A. Kabanova, M. Zschornak, T. Leisegang, V. A. Blatov, D. C. Meyer, *Chem. - Eur. J.* **2015**, 21, 16601.
- [109] P. E. Blöchl, *Phys. Rev. B* **1994**, 50, 17953.
- [110] G. Kresse, J. Furthmüller, *Phys. Rev. B* **1996**, 54, 11169.
- [111] J. P. Perdew, K. Burke, M. Ernzerhof, *Phys. Rev. Lett.* **1996**, 77, 3865.
- [112] V. I. Anisimov, J. Zaanen, O. K. Andersen, *Phys. Rev. B* **1991**, 44, 943.
- [113] S. L. Dudarev, G. A. Botton, S. Y. Savrasov, C. J. Humphreys, A. P. Sutton, *Phys. Rev. B* **1998**, 57, 1505.
- [114] A. Jain, G. Hautier, S. P. Ong, C. J. Moore, C. C. Fischer, K. A. Persson, G. Ceder, *Phys. Rev. B* **2011**, 84, 045115.
- [115] H. Jónsson, G. Mills, K. W. Jacobsen, in *Classical and Quantum Dynamics in Condensed Phase Simulations*, World Scientific, Singapore **1998**, pp. 385–404.
- [116] S. Nosé, *J. Chem. Phys.* **1984**, 81, 511.
- [117] W. G. Hoover, *Phys. Rev. A* **1985**, 31, 1695.
- [118] X. He, Y. Zhu, A. Epstein, Y. Mo, *npj Comput. Mater.* **2018**, 4, 18.
- [119] C. R. A. Catlow, *Computer Modeling in Inorganic Crystallography*, Elsevier, Amsterdam **1997**.